Infection-Specific Reprogramming of Microglia Reveals Distinct Virulence Pathways Linking Periodontal Pathogens to Alzheimer's Disease

Marta Kaminska[1], Noemie A. Dudzinska[1], Anne Klapper[2], Stefanie Geißler[2], Nadine Taudte[2], Sebastian Greiser[3], Jan Potempa[4,5], Hoger Cynis[2,6] and Piotr Mydel[1,4]

1 – Broegelmann Research Laboratory, Department of Clinical Science, Faculty of Medicine, University of Bergen, Bergen, Norway (marta.kaminska@uib.no ; noemie.dudzinska@uib.no ; piotr.mydel@uib.no)
2 - Fraunhofer Institute for Cell Therapy and Immunology, Department of Molecular Drug Design and Target Validation, 06120 Halle (Saale), Germany (anne.klapper@izi.fraunhofer.de ; stefanie.geissler@izi.fraunhofer.de ; nadine.taudte@izi.fraunhofer.de)
3 - Fraunhofer Institute for Cell Therapy and Immunology, Perlickstraße 1, 04103 Leipzig, Germany (sebastian.greiser@izi.fraunhofer.de)
4 – Department of Microbiology, Faculty of Biochemistry, Biophysics and Biotechnology, Jagiellonian University, Kraków, Poland (jan.potempa@uj.edu.pl)
5 – Department of Oral Immunity & Infectious Diseases, University of Louisville School of Dentistry, Louisville KY, USA
6 - Junior Research Group "Immunomodulation in Pathophysiological Processes" Faculty of Medicine, Martin Luther University Halle-Wittenberg, Germany (holger.cynis@izi.fraunhofer.de)

Corresponding authors: marta.kaminska@uib.no ; holger.cynis@izi.fraunhofer.de ; piotr.mydel@uib.no

ABSTRACT

Microglial dysregulation is increasingly recognized as a driver of Alzheimer's disease (AD), yet how pathogen-specific cues sculpt microglial diversity remains unclear. Here we integrate high-dimensional single-cell cytometry in vitro with spatial proteomics in vivo to dissect the impact of two major periodontal pathogens on microglia. Using a 36-marker CyTOF panel, we exposed SIM-A9 microglia to wild-type Porphyromonas gingivalis (Pg) or Tannerella forsythia (Tf) and to gingipain-deficient or S-layer–deficient mutants, resolving 38 clusters. Virulence-factor "switches" redirected cells from homeostatic states toward i) oxidative, antigen-presenting programmes driven by Pg gingipains and ii) an immunosuppressive, exhausted-like state driven by the Tf S-layer. Complementary 37-marker imaging mass cytometry of 5xFAD × hTau knock-in mice chronically infected with Pg identified 21 microglial subclusters. The cortex—but not hippocampus—lost two $Arg1^{+}$/IL-10^{+} immunoregulatory subsets (>2-fold decrease) while NADPH-oxidase-high microglia accumulated around amyloid-β and tau aggregates. These data demonstrate pathogen-specific reprogramming of microglia across model systems and brain regions, linking virulence-factor activity to AD-relevant neuroinflammation. By pinpointing gingipains and the bacterial S-layer as molecular "switches," our study highlights tractable therapeutic targets for limiting infection-driven microglial dysfunction in Alzheimer's disease.

INTRODUCTION

Neuroinflammation is a hallmark of neurodegenerative diseases, including Alzheimer's disease (AD), the most prevalent cause of dementia worldwide[1]. While inflammatory cascades in the central nervous system (CNS) were once considered secondary to neuronal loss, growing evidence now places microglia at the forefront of driving and modulating AD progression[2]. Under homeostatic conditions, these resident immune cells of the CNS support neuronal function by clearing debris and maintaining synaptic integrity. However, in AD, microglia can adopt disease-associated (DAM) states marked by excessive production of proinflammatory mediators, impaired phagocytosis, and enhanced neurotoxicity[2].

Recent single-cell and single-nucleus RNA sequencing have revealed unexpected heterogeneity within microglial populations[3,4]. Specific marker signatures distinguish these subpopulations: for instance, up-regulation of CD86 and MHC II[5,6] highlights increased antigen presentation, whereas PD-L1 (CD274) often reflects attempts to regulate T cell responses[7]. Concurrently, microglia expressing CD40 can amplify co-stimulatory signals that exacerbate neuroinflammation[8]. In contrast, TGFβ and IL-10 are frequently associated with immunoregulatory or "resting" phenotypes that safeguard neurons from inflammatory damage[9]. Enzymes such as NADPH oxidase further amplify reactive oxygen species (ROS) generation, linking chronic oxidative stress to neurodegenerative cascades[10,11]. Dissecting how these key markers change in pathological conditions is central to understanding - and potentially mitigating - the microglial contribution to AD pathogenesis.

Although multiple factors regulate these microglial transitions, a growing body of evidence implicates infectious agents as potent drivers of chronic neuroinflammation. The periodontal pathogen *Porphyromonas gingivalis* (*Pg*) has garnered special attention, given that its cysteine proteases (gingipains) have been detected in AD brains and shown to trigger neurodegeneration in animal models[12–14]. Another prominent periodontopathogen, *Tannerella forsythia* (Tf), carries a semicrystalline S-layer integral to bacterial adhesion and immune evasion and secretes an array of proteolytic enzymes potentially contributing to inflammation[15,16]. A direct impact of these virulence factors on microglial phenotypes remains poorly understood. Both organisms are implicated in periodontitis, and epidemiological and interventional studies suggest that they may contribute to cognitive decline and neuroinflammatory processes[17–19]. Periodontal disease frequently involves polymicrobial biofilms that include *Treponema denticola* or *Fusobacterium nucleatum*[20–22] and may even involve co-infection with fungi (*Candida albicans*) or viruses (HSV-1, EBV), expanding the range of microbial signatures that microglia confront[23–26]. Polymicrobial synergy can converge on shared TLR or inflammasome pathways, amplifying neuroinflammatory circuits that might predispose to AD[27–29]. Since different virulence factors likely engage distinct microglial signalling pathways - some fuelling inflammation while others skewing microglia toward immunoregulatory or "exhausted" states - elucidating these pathogen-specific effects is critical for clarifying how oral infections might influence AD progression. However, robust mechanistic data at the protein level - detailing precisely how each pathogen reshapes microglial marker expression over time - remain sparse. While transcriptomic approaches have revolutionized our understanding of microglial diversity[30], complementary high-dimensional proteomic analyses are essential for clarifying functional phenotypes and virulence factor–driven reprogramming.

In this study, we employ a 36-marker panel in cytometry by time-of-flight (CyTOF) to interrogate the phenotypic breadth of microglia exposed to *Pg* and *Tf*. By analysing wild-type strains alongside isogenic mutants (gingipain-deficient *Pg* and S-layer–deficient *Tf*), we identify virulence factor-specific pathways that shift microglia from resting or homeostatic states toward oxidative, antigen-presenting, or immunoregulatory phenotypes. We then extend these insights *in vivo*, performing spatial evaluation of microglial subpopulations in a 5xFAD x hTau-knock-in mouse model orally infected with *Pg*, using a high-dimensional imaging mass cytometry platform. Taken together, our results reveal a *Pg*-driven depletion of moderately activated microglia in favour of strong proinflammatory responses, offering compelling evidence for a contributory mechanistic link between chronic periodontitis and AD pathology - and underscoring the therapeutic and/or preventive potential of targeting specific bacterial virulence factors (e.g., gingipains) to preserve microglial homeostasis in the aging brain.

RESULTS

High-Dimensional CyTOF Profiling Reveals Extensive Microglial Heterogeneity.

We employed a high-dimensional single-cell approach *via* CyTOF with a 36-marker panel to capture the breadth of microglial phenotypes following exposure to *Pg* and *Tf* at two timepoints (24h and 48h) and two MOIs (5 and 10) using the SIM A9 microglia cell line[31]. All used antibodies were optimised and titrated in-house, with

target selectivity confirmed by staining SIM A9 stimulated with IFNγ. After de-barcoding and data pre-processing, which included gating out cell debris and beads, we downsampled all unique biological replicates to equal cell numbers.

Control (uninfected) SIM-A9 microglia primarily expressed "resting" markers (TGFβ, IL-10, CD206, Arg1), consistent with a homeostatic or surveillant phenotype in the absence of acute inflammatory stimuli (Fig. 1). Upon infection, these resting phenotypes rapidly diverged, exhibiting pathogen-specific patterns of activation, suppression, or phenotypic exhaustion. *Pg* triggered robust upregulation of proinflammatory (TNFα, IL-12p40) and oxidative markers (NADPH oxidase, iNOS), often peaking around 24 hours, while *Tf* induced a more immediate global suppression of major activation molecules (CD40, CD44, MHCII, NADPH oxidase) in certain clusters, hinting at a distinct immunomodulatory or "exhausted" route (Fig. 1).

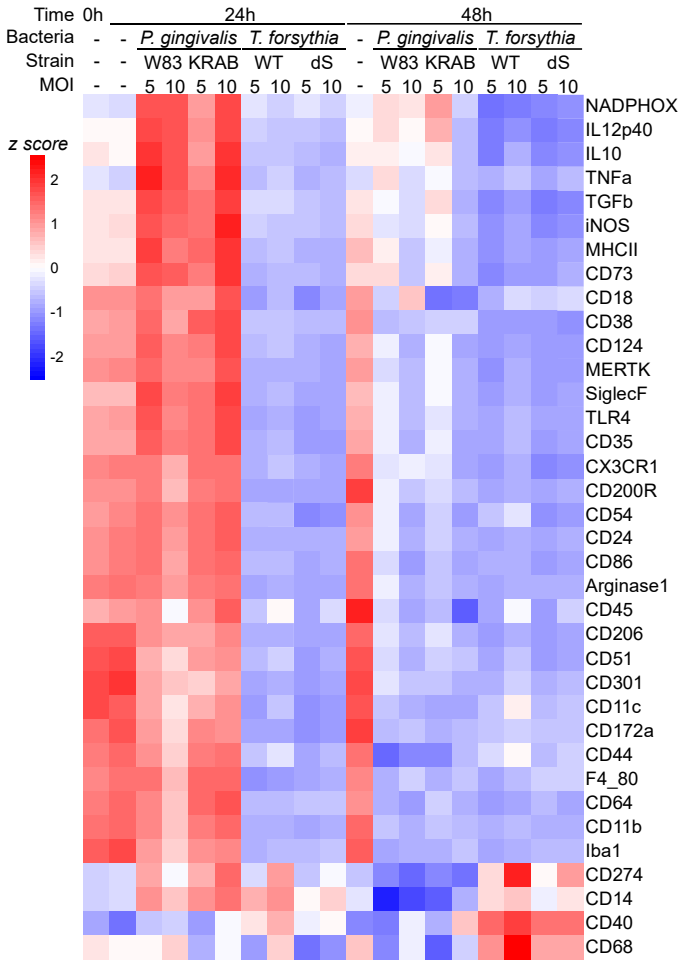

Figure 1. SIM-A9 microglia mount a rapid inflammatory burst to *P. gingivalis* and acquire an exhaustion-/senescence-like profile after *T. forsythia* infection.

Heat map of mean arcsinh-transformed, z-scored intensities for 36 CyTOF-measured protein markers in SIM-A9 microglia that were left untreated (0 h) or infected for 24 h and 48 h with either *P. gingivalis* (Pg; W83 or KRAB) or *T. forsythia* (Tf; WT or dS) at multiplicities of infection (MOI) 5 or 10. Each column is the average of all single-cell events pooled from three independent cultures per condition (745,000 cells after down-sampling); rows are hierarchically clustered. Pro-inflammatory markers (for example, TNF, NADPHOX) peak 24 h after *Pg* exposure, whereas exhaustion/senescence markers (for example, PD-L1) are preferentially up-regulated following *Tf* infection. Data are z-scored per channel across biological replicates. See Supplementary Table 1 for the antibody panel and Supplementary Fig. 1 for gating strategy.

Rapid Divergence from Homeostatic Baselines.

By using R-based Phenoannoy, we have identified 38 distinct microglial clusters, each distinguished by unique constellations of inflammatory, oxidative, antigen-presenting, and homeostatic markers (Fig. 2). In control conditions, over 60% of total microglia aggregated into clusters highly expressing the hallmark homeostatic triad (TGFβ, IL-10, CD206; Fig 2B and Extended Data Fig. 1A). Only ~10% of cells fell into mild "activation-leaning" states. Upon pathogen exposure, these resting clusters diminished—often by >70% at 24 hours ($p < 0.01$)—alongside expansions of more activated or exhausted subsets. Specifically, *Pg* infection drove marked elevations in TNFα, IL-12p40, MHCII, and iNOS, whereas *Tf* promoted broad marker downregulation, suggesting an alternative immunosuppressive or senescent microglial pathway (Fig. 2A-B). To confirm these cluster-level observations, we conducted quantitative comparisons of cluster abundance across biological replicates (Fig. 2B). Scatter plots for key clusters (Extended Data Fig. 1B) indicated significantly higher abundance enrichment under *Pg* wild-type (*Pg* WT) at MOI=10 for clusters 22, 23, 27, 35 versus control ($p < 0.05$ or $p < 0.01$) or *Tf*-infected versus control for cluster 10 ($p < 0.05$ or $p < 0.01$). Conversely, virulence-deficient mutant exposures (gingipain-deficient *Pg* KRAB, or strain *Tf* dS not producing S-layer) often yielded similar tendencies but at a reduced scale, thus suggesting full virulence is necessary for maximal proinflammatory or immunomodulatory reprogramming.

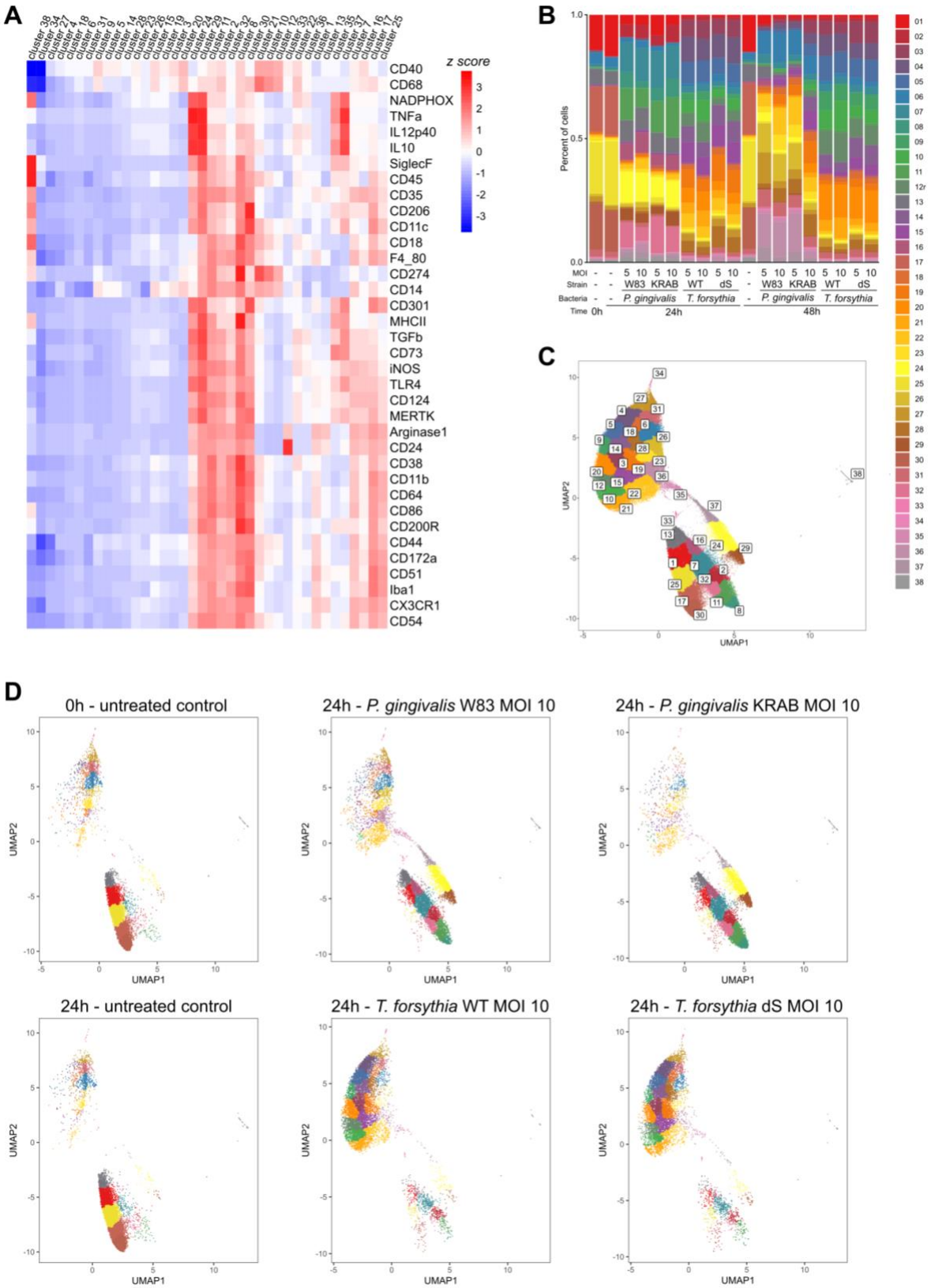

Figure 2. SIM-A9 microglia adopt discrete phenotypic states after infection with *P. gingivalis* or *T. forsythia*.

A. Heat map of z-scored, arcsinh-transformed intensities for 36 CyTOF-measured proteins across the 14 clusters identified by Phennoannoy (k = 800) from the pooled dataset of 745,000 single cells (three independent cultures per condition; see Fig. 1 and Methods). Rows are markers, columns are clusters ordered by hierarchical clustering. **B.** Relative abundance of each cluster (percentage of total cells) in untreated microglia (0 h) and after infection with *P. gingivalis* strains W83 or KRAB or *T. forsythia* strains WT or S-layer deficient (Tf dS) at multiplicities of infection (MOI) 5 or 10 for 24 h and 48 h (bars, mean ± s.d.; n = 3 biological replicates). Differences among conditions were assessed with a Kruskal–Wallis test ($P < 0.0001$) followed by Dunn's multiple-comparison correction; filled symbols indicate Padj < 0.05. **C.** UMAP projection of the concatenated dataset, coloured by cluster identity. **D.** Representative UMAPs for untreated cells (0 h) and for each MOI 10 pathogen condition at 24 h, coloured as in c, illustrate pathogen-specific redistribution of clusters.
Data derive from the same infections and CyTOF acquisition described in Fig. 1; gating, down-sampling and clustering parameters are detailed in Methods.

Time-Dependent Dynamics of Microglia upon Exposure to Periodontopathogens.
Analyses at 0, 24, and 48 hours for each experimental condition (*Pg* WT, *Pg* KRAB, *Tf* WT, *Tf* dS; MOIs 5 or 10) revealed notable heterogeneity in how cluster abundances changed over time in response to infection. Three clear patterns have emerged: (***i)*** several clusters spiked at 24 hours before returning near baseline by 48 hours (e.g., cluster 24 with high NADPH oxidase, TNFα, IL-12). This "flash and burn" motif was prominent in response to *Pg* WT (Fig. 2B, Extended Data Fig. 1C) and, to a lesser extent, in *Tf* WT infections (Fig. 2B, Extended Data Fig. 1D). For example, cluster 15, which showed $CD14^{HIGH}$ and $CD68^{HIGH}$ expression, peaked specifically in *Tf*-infected group at 24 hours and then was markedly reduced in abundance by 48 hours, illustrating an ephemeral immunomodulatory state that may later transition to an exhausted profile if pathogen exposure continues. ***(ii)*** some clusters with populations negligible at 24 hours, surged significantly at 48 hours. These late abundance clusters such as 26 and 31 —generally low in CD14/CD40—rebounded in response to infection with *Pg* KRAB or *Tf* dS, suggesting a delayed or compensatory microglial activation wave when virulence factors are absent or less potent (Fig. 2B, Extended Data Fig. 2A). ***(iii)*** finally, the abundance of cells in $Arg1^{HIGH}$ or $CD206^{HIGH}$ clusters (e.g., clusters 17, 25, 30; Fig. 2B and Extended Data Fig. 1A) decreased in response to all pathogen challenges, regardless of the expression of virulence factors. This consistent decline argues that these homeostatic microglia are not phenotypically preserved in the face of proinflammatory or immunomodulatory stressors.

***P. gingivalis* Wild Type Drives Strong Proinflammatory Polarization.**
In *Pg*–infected SIM A9 cultures, we observed high expression of canonical inflammatory and antigen-presenting markers - CD86, MHC II, TLR4, NADPH oxidase, iNOS—within certain subpopulations that peaked around 24 hours (Extended Data Fig. 1C). Clusters 24 and 29, for instance, showed elevated TNFα and IL-12p40 compared to control levels ($p < 0.01$). Comparisons at MOI 5 vs. 10 showed that higher bacterial load elicited stronger cluster expansions. By 24 hours under MOI 10, these "proinflammatory peak" clusters 24 and 29 more than doubled in proportion (Extended Data Fig. 1C). Interestingly, by 48 hours, many of these clusters returned to near- or sub-baseline expression, suggesting partial immune resolution or cellular exhaustion. Such biphasic responses likely involve initial microglial recognition of bacterial ligands (e.g., *via* TLR2/4), prompting acute cytokine and ROS release. In some subsets, including cluster 22, we detected iNOS co-expression with CD38, pointing to a state of sustained oxidative capacity with a NAD+ metabolic shift that could impact neuronal health if it persists beyond 48 hours. These dynamics emphasizes the importance of analysing multiple time points and infection doses to capture microglial complexity.

Role of Gingipains in Shaping Microglial Responses.
Comparative studies using gingipain-deficient *Pg* KRAB consistently highlighted gingipains as central drivers of the strong inflammatory shift in the infected microglia (clusters 6, 16, 23, 24, 35, 37, Fig. 2B, Extended Data Fig. 1B-C and 2B). While *Pg* WT markedly promoted the expansion of clusters expressing high levels of NADPH oxidase, TLR4, iNOS, and IL-12p40, *Pg* KRAB-infected microglia showed more muted or delayed responses. Clusters maintaining higher CD206 or TGFβ were severely diminished by *Pg* WT but persisted under

Pg KRAB, implying that gingipains help reprogram microglia from a regulatory/homeostatic phenotype to an inflammation-prone or antigen-presenting state. These data resonate with reports linking gingipains to exacerbated neurotoxicity and microglial hyperactivation[32,33], suggesting that targeting gingipains might preserve beneficial microglial subsets—an important consideration for halting pathogen-driven neurodegenerative cascades[34].

S-Layer in *T. forsythia* is a Key Inflammatory Driver.

In comparison to *Pg*, *Tf* elicited more moderate oxidative/proinflammatory shifts, but induced mild antigen-presentation phenotype (CD40, CD14, CD86) in specific clusters (i.e., 10, 12, Extended Data Fig. 1B and 2C), suggesting a different route to microglial engagement. Many *Tf*-induced changes were statistically lower in magnitude than robust expansions triggered by *Pg* ($p < 0.05$). Deleting the *Tf* S-layer (strain *Tf dS*) further reduced these moderate effects, dropping cluster abundance close to control. This aligns with the established importance of the S-layer as a major virulence factor for *Tf*. The absence of the S-layeraccelerated emergence of senescent clusters lacking typical activation markers (CD14, CD40). Hence, while *Tf* has not yet been studied in the context of the AD pathogenesis, in can be assumed that its repeated dissemination into the brain can cause low-level microglial disturbance contributing to chronic CNS inflammation. Moreover, in cluster 10 - uniquely upregulated under *Tf* WT (Fig. 2B and Extended Data Fig. 1B) - the co-expression of PD-L1, CD14 and CD68 suggested a subtle immunomodulatory axis that might alter T-cell interactions if sustained over longer time frames (Extended Data Fig. 1B). Extending infection times (beyond 48h) or applying co-infection models may help clarify *Tf*'s longer-term significance.

Convergence with Neuroinflammatory Phenotypes.

Although these in vitro data alone do not confirm the AD pathology, some cluster-level marker profiles—such as iNOS^{HIGH}, IL-12^{HIGH}, CD64^{HIGH}, or CD86^{HIGH} - overlap with neuroinflammatory or disease-associated microglia (DAM) reported in AD contexts. For instance, cluster 37, which peaked at 48 hours under *Pg* WT, aligned closely with heightened inflammatory states seen in late-stage neurodegeneration (Extended Data Fig. 2B). Our results imply that repeated or chronic exposure to periodontal pathogens could prime microglia toward the AD-like phenotypes if these inflammatory states remain unresolved.

Multilayered Functional States: Illustrative Cluster Examples.

Despite highly rigorous *in vitro* conditions, SIM A9 displayed striking heterogeneity and diverse functionality in response to pathogens and their unique patterns of virulence factors. For example, cluster 10 (CD40^{HIGH}, CD68^{HIGH}, PD-L1^{HIGH}, Extended Data Fig. 1B) was markedly upregulated after *Tf* WT infection, but completely absent in presence of *Pg*. The S-layer deletion reduced its abundance, implying the S-layer fosters immunoregulatory or checkpoint-rich microglia. Similarly, gingipain-induced cluster 24 (NADPHox^{HIGH}, IL-12^{H}^{HIGH}, IL-10^{MOD}, TLR4^{MOD}) typically exhibited highest abundance at 24 hours then waned by 48h. Cluster 35 (CD73^{HIGH}) was remarkably time-dependent, peaking at 48h in presence of *Pg* KRAB, hinting at adenosine-mediated immunosuppression emerging in the absence of gingipain-driven hyperinflammation[35]. Lastly, cluster 28 (CD14^{LOW}, CD40^{LOW}, Extended Data Fig. 1D) was observed in both *Pg* and *Tf* infections, but earlier in *Tf* and at higher abundance in the absence of S-layer, suggesting pathogen-specific timing for "exhausted/senescent" microglial states.

5xFAD x hTau KI Mice Mirrors Key *In Vitro* Findings.

Overall, our *in vitro* CyTOF data reveal that *Pg* - particularly *via* gingipains - drives potent proinflammatory or antigen-presenting microglial states, whereas *Tf*'s S-layer fosters subtler but still disruptive immunomodulatory or exhausted phenotypes. While these findings illuminate how periodontal pathogens exploit virulence factors to reshape microglial states *in vitro*, caution must be applied when extrapolating to the clinical AD setting. Immortalized lines like SIM A9 cannot fully model the interactive *milieu* of the aging brain, which includes astroglial crosstalk, neuronal signals, and peripheral immune involvement. Hence, we pursued extended *in vivo* experiments in 5xFAD mice crossed with human Tau knock-in mice- The mice generate high amyloid levels and showing pathological conformations of tau. To determine whether the pathogen-induced microglial shifts

observed *in vitro* extend to an AD-like context, the recently published 5xFAD x hTau KI mice[36] underwent a 22-week oral infection protocol with *Pg* wild type (or mock PBS). Mice were sacrificed at ~11.5 months and brains were collected, and sectioned. To facilitate comparisons between experimental groups, two brain sections per group were placed onto single slide, at a total of 4 (vehicle) or 3 brain sections (*Pg*-infected) were scanned. We analyzed sections *via* imaging mass cytometry using a 38-antibody panel overlapping with, but extending beyond, the *in vitro* set to include markers of tissue architecture (GFAP, NeuN, Cox2, GLUT1, CD13, Vcam1) that were used to identify cell types and AD lesions (amyloid, Tau, pTau). Cell-like objects were segmented (Ilastik–CellProfiler), then clustered with RPhenograph, maintaining a single-cell analytical pipeline analogous to our CyTOF approach in SIM A9 cultures.

Regional Variations and Microglial Subset Composition.

An initial characterization of segmented objects revealed region-specific differences in marker expression following infection, particularly between the cerebral cortex and hippocampus (Fig. 3A). The cortex exhibited higher baseline levels of CD40, CD13, CD172a, Arg1, and Tau, with modest increases in Iba1 and Vcam1 signals, whereas the hippocampus showed modest post-infection downregulation of GLUT1, Cox2, CD13, and CD172a. There were no significant differences between groups in total microglial frequency, microglial ROI coverage, or Iba1 antigen levels, as further confirmed by immunofluorescence imaging (Extended Data Fig. 3). Semi-supervised clustering of the Iba1^{HIGH} microglial population (Fig. 3B–E) identified 21 distinct subclusters, several of which corresponded to oxidative (NADPH oxidase^{HIGH}), antigen-presenting (CD86, MHCII), or regulatory (IL-10, Arg1) phenotypes previously observed in vitro. Most subclusters were present at similar frequencies in infected and control groups (Fig. 3F–G), suggesting subtle compositional shifts rather than global expansion or depletion of microglia.

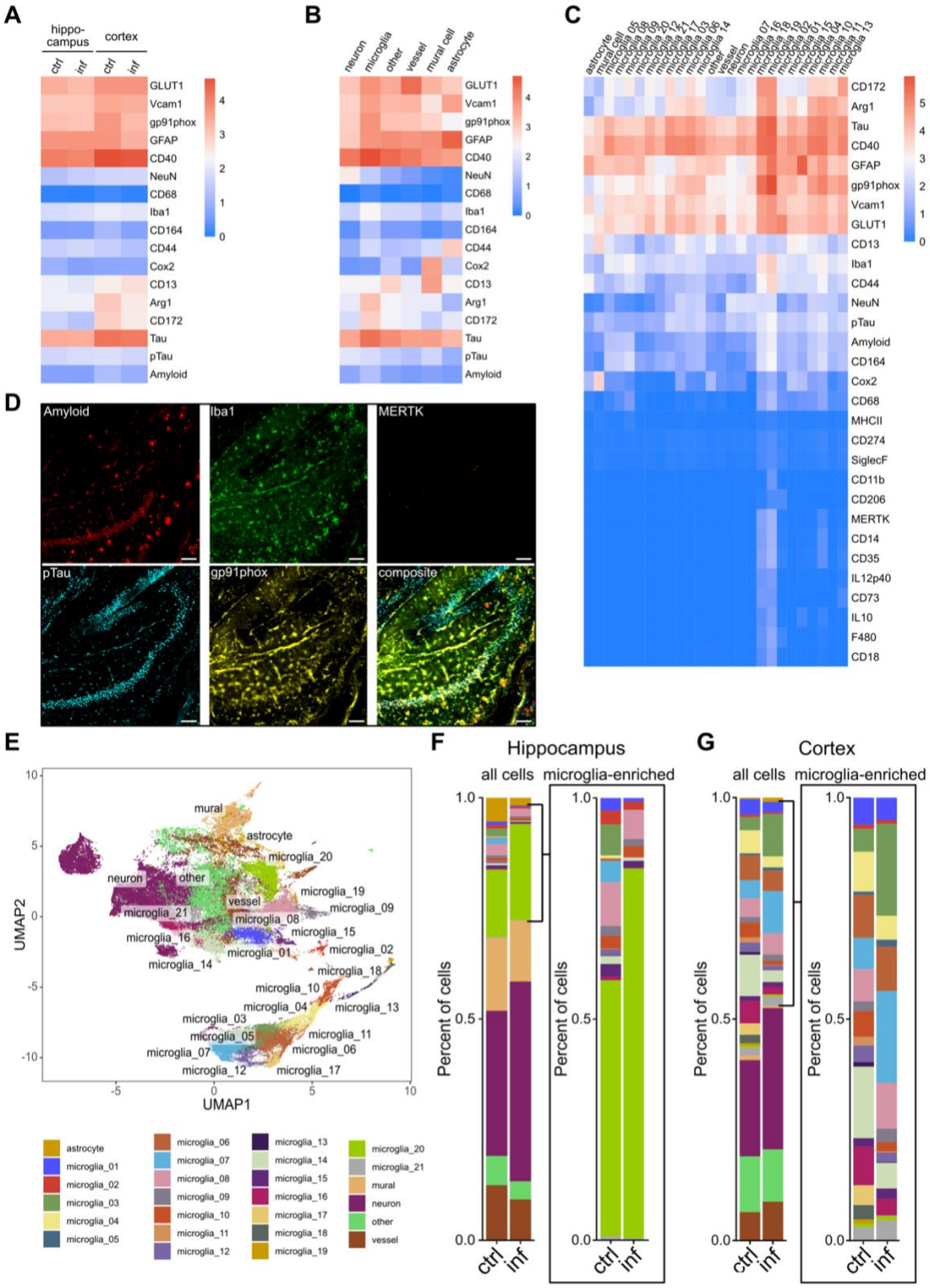

Figure 3. Region-specific microglial phenotypic shifts following chronic *P. gingivalis* exposure in hTau-knock-in × 5×FAD mice.

A. Heat map showing arcsinh-transformed, z-scored expression of 17 imaging mass cytometry markers across all initial Rphenograph-derived clusters (k = 50; n = 78,622 cells). Columns represent individual imaging subgroups, and rows denote marker intensity. **B.** Marker expression heat map of broad cell classes identified by cluster-level profiling. Cell types were assigned based on characteristic marker patterns: NeuN^{HIGH} (neurons), Iba1^{HIGH} (microglia), GLUT1^{HIGH} (endothelium), GFAP^{HIGH} (astrocytes), CD13/COX2^{HIGH} (mural cells), and 'other' (unclassified). **C.** Heat map of arcsinh-transformed, z-scored marker expression across 21 microglial subclusters derived from secondary clustering (k = 60) of Iba1^{HIGH} cells. **D**. Representative hippocampal image from the IMC dataset showing single-channel expression of Aβ (amyloid), Iba1, MERTK, pTau (AT8), and gp91phox, with composite overlay (far right). Scale bar, 100 μm. **E.** UMAP representation of batch-corrected events, coloured by the 21 subclusters defined in c, highlighting the phenotypic redistribution of microglia following infection. **F.** Relative abundance of microglial subclusters in hippocampus, displayed as proportion of total segmented events (mean per group). Group comparisons performed with Kruskal–Wallis test with Dunn's post hoc correction; Padj < 0.05 were considered significant. **G.** As in F, but for cerebral cortex, revealing region-specific subcluster enrichment. Data are from PBS-treated control mice (n = 4) or *P. gingivalis*–infected mice (n = 3) after 22 weeks of oral challenge. Tissue processing, staining, denoising, segmentation, clustering, and statistical methods are described in detail in Methods.

However, the cortical microglial landscape showed a significant depletion of two subsets - microglia 10 and microglia 14 - in infected mice (Fig. 3G, $p < 0.05$, Kruskal–Wallis with Dunn's post-hoc). Microglia 10 displayed a regulatory profile (relatively high Arg1, CD40, moderate IL-10, MERTK, CD14, CD35, MHCII), closely resembling the "mixed" or modestly activated subpopulations suppressed by *Pg in vitro*. Microglia 14, conversely, lacked IL-10, MERTK, or CD14 and showed low MHCII. Abundances of both were reduced more than two-fold in infected samples vs. controls, indicating a loss of immunomodulatory or mild-activation microglia in the cortex. In contrast, hippocampal microglia composition remained comparatively stable and arguably more homogenous (more than 50% of identified microglia belonged to subcluster 20) apart from moderate abundance increase in microglia 20 (CD172a^{LOW}, Arg1^{LOW}, CD40^{MOD}), which partially parallels the "milder" or "exhausted" *in vitro* phenotypes observed under *Tf* exposure. These data indicate that hippocampal microglia possess region-specific thresholds for infection-driven reprogramming.

Spatial Interactions and Protein Aggregate Association.

To understand how these altered subpopulations might interact with the local environment, we examined cell-type–enriched regions (Fig. 4A-C) dominated by blood vessels (region 1), astrocytes (2), neurons (3), "other" cell types (4), mural cells (5), or microglial subclusters (6). Comparing their relative frequencies pre- vs. post-infection revealed that in the cortex, the ratio of "non-interacting" microglia (region 6 in spatial context 6 containing majority of the microglial subsets) decreased (from ~0.35 ± 0.05 to ~0.25 ± 0.04, $p < 0.05$), while spatial contexts (SCs) of neurons and microglia_21 interacting with microglia_08, _15 and "other" cell types (SC 3_4), but also with blood vessels and microglia_02 (SC 1_3_4) increased post Pg-infection (Fig. 4D). Clusters reminiscent of "flash-and-burn" microglia (e.g., microglia 8, 15, 21) became more prevalent in these multi-cell contexts, suggesting an increased immune engagement and cellular crosstalk post-infection. In parallel, microglial clusters 10 and 14, depleted during oral infection, were predominantly assigned to the non-interacting microglial context (SC 6, Fig. 4E). SC 4_6, harbouring microglia 14, was depleted in the cerebral cortex post-infection, similarly to SC 3_4_6 in hippocampus. In contrast to the changes observed for cortices, SC 3_4 was slightly depleted post-infection, similarly to SC 1, 1_6 (interaction between blood vessels+microglia_02 and microglia regions) and 5 (comprised of mural cells). Moreover, a hippocampal enrichment in SC 3 was observed post-infection, which was predominantly composed of neurons and approx. 50% of microglial subcluster 21, and to a smaller degree increase in abundance of SC 1_5 (blood vessels - mural cells) and 3_6 (neurons - microglia_20, the subcluster dominating in hippocampus). Although hippocampal changes were not as pronounced, the region harboured potential "compensatory" microglial subsets that appeared to resist infection-driven depletion.

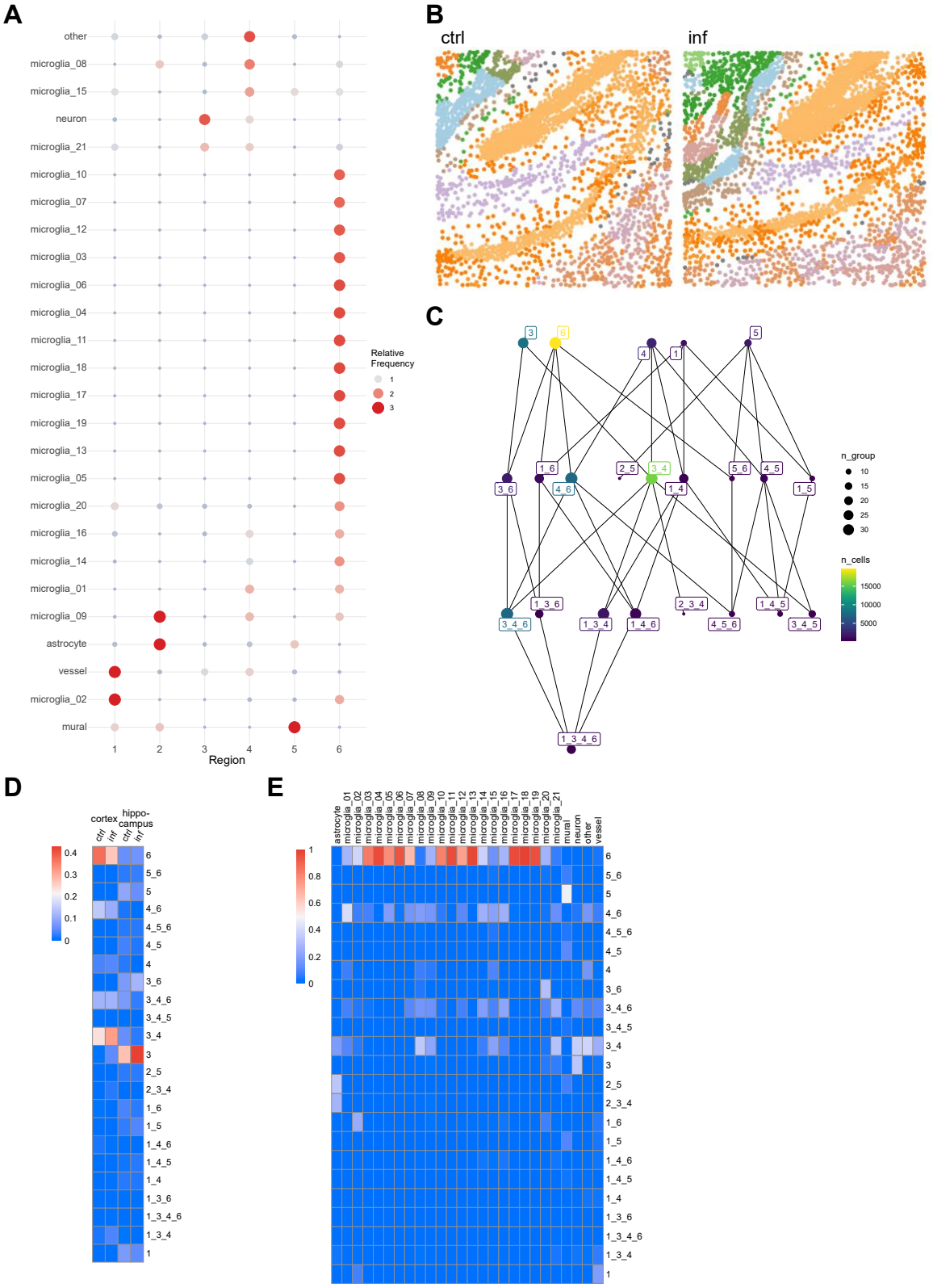

Figure 4. Chronic P. gingivalis infection alters spatial microenvironments in hTau-knock-in × 5×FAD mice.

A. Segmented objects were assigned to one of six major cell-type–enriched regions (NeuN^{HIGH} neurons, Iba1^{HIGH} microglia, GFAP^{HIGH} astrocytes, GLUT1^{HIGH} endothelium, CD13/COX2^{HIGH} mural cells, and undefined "other") *via*

expansion algorithm (radius = 40 px) based on full clustering (major cell types, with microglia further subclustered. **B.** Representative hippocampal ROIs from a PBS-treated control (left) and infected (right) mouse, with spatial contexts (SCs) shown in unique colors. SCs were defined using a k-nearest neighbor (k = 40) approach based on cellular proximity and composition. **C.** Overview of SC identities and their interrelationships, combining all retained ROIs (≥5 ROIs per SC, ≥200 total objects per SC). **D.** Frequencies of individual SCs per brain region and experimental group, shown as the proportion of all SCs within that category. **E.** Proportions of each identified cluster (21 microglial subclusters plus 5 remaing main cell types) within each SC, expressed relative to the total number of cells assigned to that SC.
SCs were constructed by spatial graph modeling using imcRtools, followed by compositional and contextual analysis via lisaClust. Low-frequency SCs (occurring in <5 ROIs or with <200 cells total) were excluded from analysis.

To evaluate AD lesion interactions, we segmented the protein aggregates into four categories: (1) amyloid^{HIGH}; (2) pTau (pTau^{HIGH} with NeuN^{HIGH}); (3) pTau_d (pTau^{HIGH} but NeuN^{LOW}); and (4) mixed (amyloid^{HIGH} and pTau^{HIGH}) (Fig. 5A, D-E). Heatmap analyses of these lesions (23 chosen antigens) showed amyloids often induced robust Iba1 infiltration (implying strong microglial presence), while mixed lesions contained the highest gp91phox and CD40 signals, consistent with a potent oxidative or antigen-presenting environment. Proximity analyses (Fig. 5B–C) highlighted the microglia subset 10 as infiltrating the pTau- or amyloid-rich regions, with subset 14 more frequently observed at the lesion border. We then further performed proximity interaction analysis, which confirmed these observations: subset 10 exhibited highest interaction score with mixed-type lesions of all microglial subsets, pointing to a critical role of this subset in lesion formation or maintenance (Fig. 5F). Notably, microglia 10 and 14 - both diminished under infection - were strongly associated with mixed lesions in controls (Fig. 5F), suggesting they play roles in containing or regulating combined amyloid–pTau pathology. In fact, with depletion of subset 10 and 14 in cerebral cortex post-infection, we have observed lower abundance of mixed lesions altogether, in favour of pTau (both NeuN^{HIGH} and NeuN^{LOW}). Their infection-driven decline could thereby compromise lesion handling or local immune homeostasis. However, the protein aggregate coverage in cerebral cortex remained comparatively stable, as opposed to hippocampus, were total area occupied by these proteinaceous lesions was increased post-infection (Fig. 5D-E).

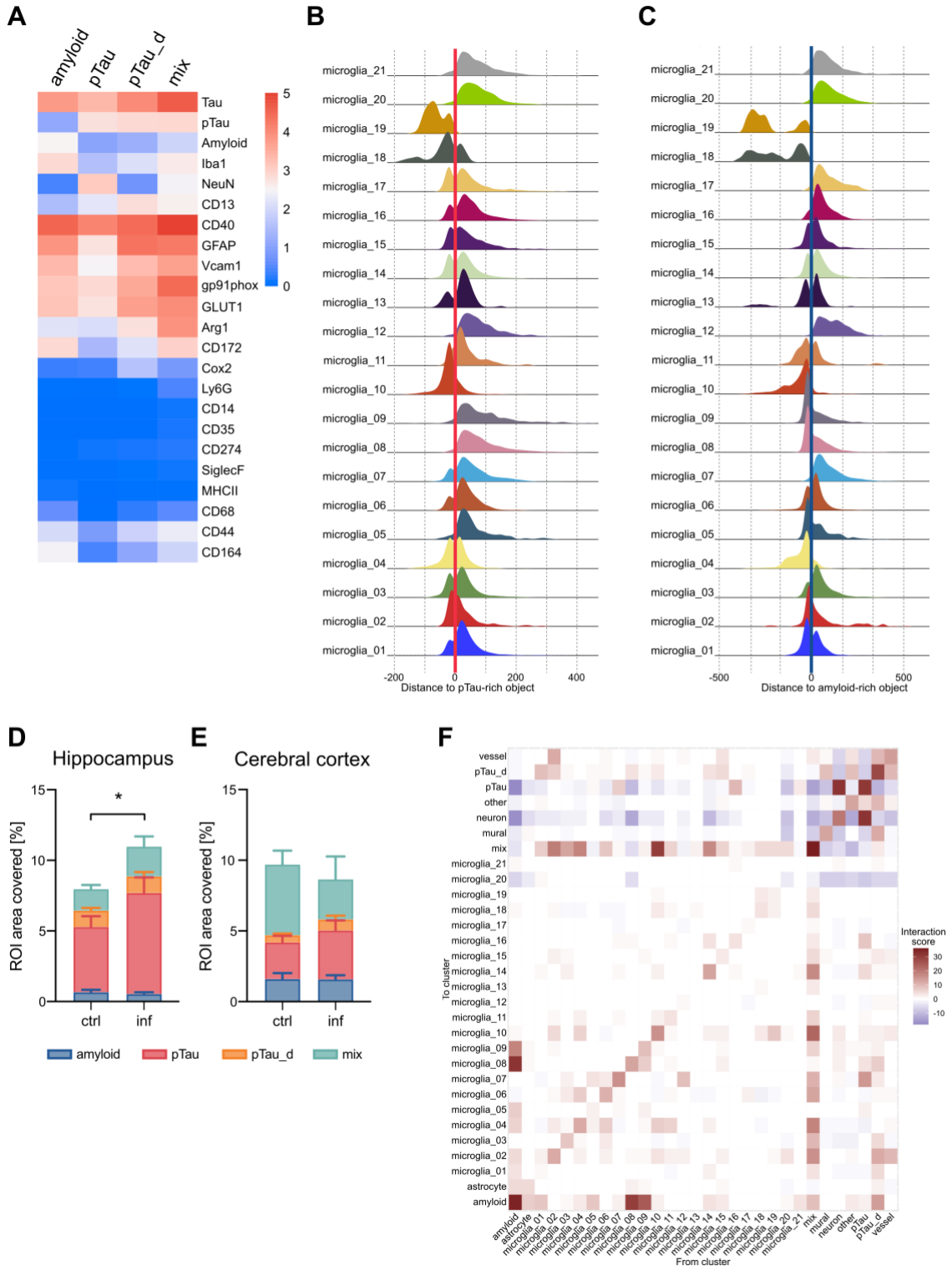

Figure 5. Local cell–aggregate interactions are reshaped in chronically infected hTau-knock-in × 5×FAD mice.

A. Harmony-integrated UMAP of 60 258 segmented non-cellular objects (see Methods) coloured by four aggregate classes derived by Rphenograph clustering (k = 60): $A\beta^{HIGH}/pTau^{LOW}$, $pTau^{HIGH}/A\beta^{LOW}$, $pTau^{HIGH}$ + $NeuN^{HIGH}/A\beta^{LOW}$, and mixed $A\beta^{HIGH}$ + $pTau^{HIGH}$. **B.** Density plot of microglia ($Iba1^{HIGH}$) subclusters as function of distance to $pTau^{HIGH}$ patches (threshold ≥ 2.35 × background; patch edge = 0 µm). Distance distributions show

the number of objects (cells) as a function of their distance from the edge of pTau^{HIGH} patches. **C.** As in b, but for high-amyloid patches (threshold ≥ 1.5 × background). **D.** Percentage of ROI area occupied by pTau or amyloid aggregates in hippocampus and cortex (bars, mean ± s.d.). Cumulative aggregate coverage is higher in infected mice in hippocampus (Mann Whitney two-tailed, $p = 0.0357$); in cerebral cortex aggregate coverage is unchanged ($p = 0.39$). **E.** Heat-map of asymmetric interaction scores (imcRtools testInteractions, patch radius = 3 cells, expansion = 20 px) between the 21 microglial subclusters, other major cell classes, and each aggregate class. Positive enrichment (red) and spatial avoidance (blue) are coded by the summed significance value (Σ sigval; Methods). Infected tissue shows strengthened contacts between disease-associated microglia subclusters and mixed Aβ/pTau aggregates, and reduced contacts between NeuN^{HIGH} debris and homeostatic microglia. Aggregate segmentation, patch detection, proximity and interaction analyses were performed as detailed in Methods; low-frequency patches (< 6 px) were excluded.

Interestingly, the NADPHox^{HIGH} subsets 18 and 19, similar to the highly activated "flash-and-burn" microglia *in vitro*, were strongest infiltrators of both pTau and amyloid rich regions, but their interactions scores with these types of aggregates remained modest. In the hippocampus, microglia 20 remained relatively distant from amyloid/pTau^{HIGH} lesions, with microglia subset 1 as the dominant hippocampal responder to the protein aggregates. These differences reinforce our earlier observation on the region-specific differences in microglial heterogeneity and functionality.

Linking *In Vitro* and *In Vivo* Pathogen Effects.

These *in vivo* data validate and extend the *in vitro* findings in a disease-relevant setting. The selective depletion of moderately activated/regulatory subsets (microglia 10, 14) in the cortex under *Pg* infection strongly correlates with the in vitro phenomenon in which *Pg* WT suppresses Arg1^{HIGH}, IL-10^{HIGH} microglia. Moreover, the infiltration of more proinflammatory or oxidative subpopulations around amyloid/pTau aggregates parallels the *"flash-and-burn"* phenotypes induced by gingipains *in vitro*. Although hippocampal shifts were subtler, the in vivo data highlight region-specific vulnerabilities—potentially aligning with early cortical AD pathology or distinct local microenvironments. Although *Tf* was not assessed *in vivo*, the partial parallels in hippocampal microglia underscore how different pathogens might preferentially reprogram distinct brain regions if tested in multi-infection models.

Overall, chronic *Pg* infection in an AD-prone environment (5xFAD x hTau KI mice) leads to a net erosion of regulatory microglial subpopulations critical for immunomodulation (Arg1^{HIGH}, IL-10^{HIGH}, MERTK^{HIGH}), while fostering subsets that localize around pathological aggregates, potentially exacerbating lesion growth or neuroinflammation. These findings provide novel region- and lesion-specific insights into how oral pathogens may synergize with AD pathology and strengthen the case for therapeutic gingipain inhibitors or other antimicrobial strategies aimed at preserving beneficial microglial subsets in aging brains.

DISCUSSION

Microglia, the resident immune cells of the CNS, have increasingly been recognized as pivotal regulators of AD, capable of both protective and detrimental effects depending on their activation states and the local environment. Advances in single-cell profiling - particularly single-cell RNA-sequencing and high-dimensional cytometry - have revealed a complex spectrum of microglial phenotypes, challenging the once-binary view of "resting" *vs.* "activated" microglia[37,38]. Even in homeostatic conditions, microglia are a highly heterogeneous and adaptable population, with their diversity shaped by regional specialization, proximal cell signals, and systemic influences[30,39]. Despite these insights, much remains unknown about how oral pathogens, especially *Pg* and *Tf*, drive microglial diversity at high resolution. Our study addresses this critical gap by systematically dissecting pathogen-specific microglial phenotypes both *in vitro,* with comprehensive CyTOF analyses, and *in vivo*, using imaging mass cytometry in a mouse model recapitulating hallmarks of AD.

We identified 38 distinct microglial clusters in our *in vitro* experimental model using SIM A9 murine cell line, reported to harbour primary-like phenotypes. *Pg* WT induced robust inflammatory bursts, potentially exacerbating AD-like pathology *via* excessive NF-κB activation[40,41]. Further supporting our data, a previous report highlighted *Pg*'s ability to activate PAR2, resulting in preferential up-regulation of proinflammatory mediators, while not significantly elevating regulatory molecules such as IL-10, effectively impairing microglial self-regulatory mechanisms[42–44]. Conversely, *Tf* drove a faster but more sustained dampening consistent with an "exhausted" phenotype - indicating that specific virulence factors (e.g., gingipains, LPS, fimbriae in *Pg*, the S-layer and plethora of proteases in *Tf*) differentially skew microglial function. Comparisons with isogenic mutants (*Pg* KRAB, *Tf* dS) underscored that discrete bacterial proteins act as "molecular levers," pivoting microglia between proinflammatory or moderately immunoregulatory states. Such high-dimensional mapping - unprecedented for these pathogens - refines a field where prior work relied on incomplete marker sets or generalized infection models, obscuring the finer details of microglial dynamics.

Our data also clarifies that the presence or absence of gingipains (in *Pg*) or the S-layer (in *Tf*) consistently dictates both the severity and trajectory of microglial activation. Our data support the hypothesis that gingipain-mediated microglial activation intersects with established AD pathways - enhancing oxidative stress (NADPH oxidase, iNOS) and upregulating TLR4, MHC II, co-stimulatory molecules (CD86)[45–47]. These disease-associated microglia have been implicated in AD murine models, often converging around plaques and fuelling ongoing neuroinflammation[48,49]. *Pg* strain lacking gingipains (*Pg* KRAB) exhibited blunted inflammatory states, preserving regulatory subsets such as CD73^{HIGH} or IL-10^{HIGH} microglia - crucial for immunoregulation. Meanwhile, *Tf* S-layer deficiency abrogated its capacity to elevate antigen-presenting (CD40, MHC II) or checkpoint-rich (PD-L1/CD274) microglia suggesting that certain checkpoint-oriented phenotypes require intact S-layer signals[50]. While immune checkpoints typically limit T-cell activation, they could paradoxically maintain smouldering inflammation if they curb microglial–T-cell clearance of misfolded proteins[51–54]. Together, these observations reinforce that microglial phenotypes are carefully orchestrated by pathogen proteins, guiding novel therapeutic strategies (e.g., gingipain inhibitors).

In vivo, we employed imaging mass cytometry in hTau-knock in 5xFAD mice to see whether the pathogen-driven *in vitro* phenotypes persist under AD-like conditions. Remarkably, chronic *Pg* infection selectively reduced cortical microglial clusters (e.g., subclusters 10, 14) characterized by moderate MHC II, CD86, and IL-10, mirroring our *in vitro* finding that gingipains erode homeostatic or "mixed" microglia, thus impairing regulatory mechanisms and further propelling AD-like pathology. Intriguingly, prior reports indicate that other chronic infections (e.g., COVID-19) also heighten proinflammatory responses at the expense of moderate immunomodulatory phenotypes, underscoring that sustained inflammatory stimuli frequently displace beneficial or intermediate states[55–57]. Furthermore, we observed that these moderately activated subpopulations (high levels of CD14, CD35, CD68, MERTK) interacted strongly with mixed aggregates (amyloid^{HIGH} and pTau^{HIGH}), implying they attempt to phagocytose or regulate lesion growth without causing neurotoxicity[58,59]. Their depletion under infection likely accelerates neurodegenerative lesions, echoing the synergy between chronic inflammation and protein aggregation.

Our spatial analyses confirmed region-specific differences in microglial subcluster composition—cortex vs. hippocampus - consistently aligning with prior hypotheses that region-specific microglial makeups underlie differential vulnerability to aging and pathological stressors[60–62]. Since hippocampal changes were comparatively subtle here, we posit that the relatively advanced disease stage (~11 months) in our 5xFAD x hTau knock-in mice might eclipse potential earlier hippocampal shifts. Future studies employing younger mice or extending the infection timeline could better distinguish AD *vs.* infection-specific microglial alterations in the hippocampus.

These data tighten the link between oral pathogen infection and AD-relevant microglial reprogramming, bridging two previously disconnected research domains: periodontal infection and microglial heterogeneity in

435 AD. Therapeutically, our findings resonate with the promise of gingipain inhibitors and highlight potential
436 benefits of targeting *Tf*–specific factors (S-layer), especially if multi-pathogen synergy ultimately proves critical
437 in AD progression. Future work exploring co-infections (e.g., *T. denticola*, *F. nucleatum*, or fungal/viral species)
438 may uncover further microglial states or synergies that accelerate - or possibly mitigate - AD pathogenesis.
439 Our findings also highlight the power of spatial proteomics—unlike conventional immunofluorescence, this
440 approach enabled precise mapping of microglial subtypes potentially critical to AD pathogenesis. By capturing
441 multiple functional markers simultaneously, our mass cytometry pipelines exceed single-marker approaches,
442 unveiling unprecedented microglial plasticity under infection stress. This broad, integrated view illuminates how
443 discrete microglial subsets fluctuate depending on which bacterial virulence factors predominate - and how
444 these shifts coincide with AD lesion development. Additionally, our protein-level focus circumvents
445 transcriptome-proteome mismatches that can complicate single-cell RNA-seq analyses in aged or diseased
446 brains[63–65]. Hence, this study provides a conceptual and methodological platform for dissecting oral pathogen–
447 microglia interactions, bolstering the rationale that targeting microbial virulence (gingipains, S-layer) might help
448 alleviate microglial dysregulation and decelerate AD progression.
449 Nonetheless, open questions remain. Longitudinal *in vivo* imaging or serial sampling will clarify whether
450 pathogen-induced microglial changes directly accelerate plaque or tangle formation, and whether early blockade
451 of gingipains or S-layer can spare crucial immunoregulatory microglia and improve cognitive outcomes. Overall,
452 our findings accentuate that microglia, far from bystanders, actively detect bacterial virulence signals in their
453 vicinity and transition into states consistent with heightened or chronic neuroinflammation. By reconstructing
454 these pathogen-specific microglial responses at single-cell resolution—both *in vitro* and in an AD-like
455 environment - we illustrate how oral pathogens globally alter microglial heterogeneity, merging periodontal
456 research with the evolving landscape of AD immunopathology. This synergy reveals actionable mechanistic
457 pathways for future interventions aimed at neutralizing virulence factor–driven neuroinflammatory cascades,
458 offering rational therapeutic designs to complement established anti-amyloid or anti-tau strategies.
459 Finally, by coupling a high-dimensional *in vitro* model with a 5xFAD x hTau KI system, we demonstrate that
460 *Pg* and *Tf* exploit distinct virulence factors - gingipains and S-layer - to reprogram microglial subsets along
461 proinflammatory, antigen-presenting, or immunoregulatory axes, validating that infection-driven heterogeneity
462 indeed applies under AD-like conditions. These insights move beyond monolithic views of "activated"
463 microglia, identifying pathogen-derived molecular "switches" as promising targets to contain infection-driven
464 neuroinflammation in Alzheimer's disease.
465
466
467 **Materials and Methods**
468 **Bacteria culture**
469 *Porphyromonas gingivalis (Pg)* W83, gingipain-deficient *Pg* ΔKgpΔRgpAΔRgpB in W83 background (KRAB),
470 *Tannerella forsythia (Tf)* ATCC 43037 and non-S-layer-producing *Tf* were cultured on BD BBL Brucella agar
471 (Beckton Dickinson; 211086) plates supplemented with hemin (SigmaAldrich, H9039), vitamin K
472 (SigmaAldrich, M5625), and 5% defibrinated sheep's blood, under anaerobic conditions at 37°C. For *Tf*, agar
473 medium was additionally supplemented with N-acetylmuramic acid (0.01 mg/ml; SigmaAldrich, A3007).
474 Bacteria were passaged onto fresh agar every 48h (*Pg*) or 120h (*Tf*). For the *Pg* KRAB strain, agar plates
475 contained tetracycline (1 μg/ml; SigmaAldrich, T7660) and erythromycin (5 μg/ml; SigmaAldrich, E5389).
476 Bacterial suspensions for microglia infections were prepared by suspending freshly cultured bacteria (≤48h for
477 *Pg*, ≤72h for *Tf*) in sterile PBS, followed by centrifugation (4600 rpm, 10 min, 4°C). After resuspension in PBS,
478 bacterial aggregates were removed by low-speed centrifugation (800 rpm, 5 min, 4°C). Optical density (OD_{600})
479 was measured, and colony-forming units (CFUs) were estimated (*Pg*OD_{600} = 1 corresponding to 1×10^9
480 CFU/ml; *Tf* OD_{600} = 1 corresponding to 6.8×10^8 CFU/ml).
481

482 **Cell line culture**

483 The murine microglial SIM-A9 cell line (ABM, T0247) was cultured in DMEM/F12 (ThermoFisher, 31331093)
484 containing 10% FBS (ThermoFisher, A5256801), 5% horse serum (ThermoFisher, 16050), 100 U/ml penicillin,
485 and 100 μg/ml streptomycin (ThermoFisher, 15140122), at 37°C in a 5% CO_2 humidified incubator. Cells were
486 passaged by pooling suspension and adherent fractions, followed by trypsinization, centrifugation (280g, 10
487 min, RT), and resuspension in fresh medium. Cells were seeded at a 1:10 dilution; passages 5 and 6 were used
488 for infection experiments. Cell density was measured using trypan blue exclusion on a Bürker chamber.

489

490 **Microglia infection**

491 SIM-A9 cells were seeded at 5.33×10^5 cells/ml in 6-well plates and allowed to adhere overnight (16h). Before
492 bacterial challenge, the medium was replaced with serum- and antibiotic-free DMEM/F12, and cells were
493 incubated for an additional 2h. Bacteria were introduced at multiplicities of infection (MOI) of 5 or 10. Cells
494 collected at 0h (pre-infection) were washed with PBS, while infected cells were harvested at 24h and 48h.
495 Cell suspensions were centrifuged at 300g for 5 min in RT and resuspended in PBS. Samples were centrifuged
496 (300g, 5 min in RT), resuspended in Maxpar Cell Staining Buffer (Standard Biotools, 201068). Fixing and
497 barcoding were perfomed according to the manufacturer's instruction. Cells were fixed in 4% paraformaldehyde
498 (PFA; ThermoFisher, 28908) diluted in PBS for 5 min, washed in Barcode Perm Buffer (Standard Biotools,
499 201057) and stained with barcodes: Pd-102, Pd-104, Pd-105, Pd-106, Pd-108, Pd-110 (Cell-ID 20-plex Pd
500 Barcoding kit, Standard Biotools, 201060) in Barcode Perm Buffer for 30 min in RT. Some samples were
501 additionally stained with 20 nM cisplatin (cisPt195, Neonest AB) to increase sample pooling capacity. Barcoded
502 cells were then washed in Maxpar Cell Staining Buffer and pooled together for antibody staining.

503

504 **Polymer conjugation**

505 All antibodies, except those purchased directly from Standard Biotools, were conjugated to metal-chelating
506 polymers in-house. Conjugating kits for: 144Nd, 145Nd, 146Nd, 147Sm, 148Nd, 149Sm, 150Nd, 152Sm,
507 155Gd, 158Gd, 160Gd, 161Dy, 162Dy, 163Dy, 165Ho, 166Er, 167Er, 168Er, 169Tm, 173Yb, 175Lu, 176Yb
508 were purchased from StandardBiotools, while kits for: 115In, 170Er and 171Yb were purchased from Ionpath.
509 All conjugations were performed according to the respective manufacturer's instruction. For each conjugation,
510 antibodies (100 μg per conjugation) were used without bovine serum albumin (BSA). Antibody protein
511 concentrations were measured using NanoDrop spectrophotometer at 280 nm before and after conjugation.
512 Final concentrations were adjusted to 0.5 mg/ml in Antibody Stabilizer with HRP-Protector™ (Candor
513 Bioscience, 220 050) for suspension staining, or in manufacturer-provided buffer (Ionpath) for imaging mass
514 cytometry. All conjugates were stored at 4°C.

515

516 **Antibody panels: titration and validation**

517 Prior to experimental use, all antibodies were rigorously titrated on SIM A9 cells. Cells were fixed, then blocked
518 using anti-mouse CD16 antibody (1 μg per 3 million cells, BioLegend, cat. 101302) for 10 min at room
519 temperature (RT). Serial antibody dilutions ranging from 1:100 to 1:3200 were applied to the cells and incubated
520 for 30 min at RT. Cells were subsequently washed with Maxpar Cell Staining Buffer and fixed again with 4%
521 PFA for 5 min at RT. For antibodies targeting intracellular proteins (TNFα, IL-10, IL-12p40, TGFβ, Arg1,
522 NADPH oxidase, and iNOS) cells underwent permeabilization with Maxpar Perm-S Buffer (Standard Biotools,
523 201066) for 30 min at RT, followed by intracellular antibody staining for 30 min at RT. After staining, cells
524 were washed once more in Maxpar Cell Staining Buffer, fixed in 1.6% PFA for 10 min, and nuclei were stained
525 with Cell-ID Interacalator (Standard Biotools, 201192A) at 31.25 nM for 1h. For signal acquisition, cells were
526 suspended in Maxpar Cell Acquisition Solution Plus (Standard Biotools, 201244). For antibody selectivity
527 confirmation, SIM A9 cells were stimulated with 100 ng/ml recombinant murine IFNy (StemCell, 78021.1) for
528 16h prior to antibody staining. Data was collected as described in the Data Collection section. The optimal
529 dilution for each antibody was identified as the dilution providing clear signal intensity above the minimal
530 detectable threshold but significantly below the maximal point of the dynamic range (Supplementary Fig. 1A-
531 B).

532 For imaging mass cytometry, staining was performed as described below using OCT-embedded brain sections
533 (thickness 10 μm) prepared from C57BL/6 wild-type mice. For titration procedure, 1:50 – 1:200 dilutions were
534 tested, and all antibodies were incubated with tissues for 16h in 4°C. When antibody signal-to-noise ratio was
535 deemed sufficient on visual inspection, antibody selectivity was inspected based on previously established
536 expression patterns and tissue architecture. Titrated antibodies that passed this initial inspection were then
537 validated on liver sections (thickness: 10 μm) selected for their abundance of Kupfer cells. Antibodies that
538 exhibited differential and anatomically appropriate expression patterns across brain and liver tissues were
539 confirmed as validated and included in subsequent imaging mass cytometry analyses (Supplementary Fig. 1D).
540

541 **Data collection**

542 Barcoded and pooled SIM A9 were blocked with anti-mouse CD16 (1 μg/3 million cells, BioLegend, cat.
543 101302), and stained with antibody cocktail (Supplementary Table 1, surface markers). Cells were washed briefly
544 in Maxpar Cell Staining Buffer, fixed again (4% PFA in PBS, 5 min in RT), permeabilised with Maxpar Perm-
545 S Buffer and then stained with intracellular marker antibody cocktail (Supplementary Table 1) diluted in Maxpar
546 Perm-S Buffer for 30 min in RT. Then, cells were washed once again in Maxpar Cell Staining Buffer, fixed in
547 1.6% PFA for 10 min and nuclei were stained with Cell-ID Interacalator at 31.25 nM for 1h.
548 For signal acquisition, cells were suspended in Maxpar Cell Acquisition Solution Plus and strained (Falcon,
549 352235). Cells were pelleted (800 g for 2 min in 4°C) and pellets were loaded onto CyTOF instrument, where
550 they were suspended in Maxpar Cell Acquisition Solution Plus at 0.75 mln/ml density. EQ™ Six Element
551 Calibration Beads (33,000 beads/ml; StandardBiotools) were added and signal was recorded at speed of 200 –
552 350 events/s using CyTOF XT (Standard Biotools), operated by CyTOF software 8.1.0 (Standard Biotools).
553 Bead-based signal normalisation and initial event debarcoding was performed using CyTOF software and
554 Debarcoder algorithm with provided barcode key as a .csv file with Maximum Amhalanobis Distance = 10.
555 Generated data was then expored as .fcs files for further processing.
556

557 **Data preprocessing**

558 Initial processing was performed in FlowJo v10.8.1 (Beckton Dickinson). Samples were gated for cisplatin-
559 based barcodes, and EQ bead events (140Ce) were excluded. Doublets (Ir191 vs Ir193) and debris (Ir191 vs
560 event length) were also removed (Supplementary Figure 1C). Clean .fcs files were imported into R
561 (SingleCellExperiment v1.26.0, flowCore v2.16.0), transformed using an inverse hyperbolic sine function
562 (asinh, co-factor = 5). Subsequently, samples were downsampled to equalize event counts across biological
563 replicates, resulting in a final dataset comprising 745,000 cells in total. No spillover compensation was
564 performed on this dataset.
565

566 **Clustering**

567 Uniform Manifold Approximation and Projection for Dimension Reduction (UMAP) was generated.
568 Phenoannoy[66] (0.1.0, at k=800) was used for unsupervised clustering, as number of events exceeded
569 computational power required to employ Rphenograph package, while FLOWsom package did not provide
570 sufficient resolution to highlight microglial heterogeneity *in vitro*.
571

572 **Animals**

573 Generation of 5xFAD x hTau KI mouse model was described in Barendrecht et al 2023[36]. All animal
574 experiments were approved by the responsible animal ethics committee of the state of Saxony-Anhalt, Germany
575 (Landesverwaltungsamt Sachsen-Anhalt, Department of Consumer Protection and Veterinary Affairs, Halle
576 (Saale), Saxony-Anhalt, Germany) under the following approval numbers: 42502-2-1371 MLU and 42502-2-
577 1670 IZI.
578 Fifty μl containing either 10^9 CFU *Pg* (strain ATCC 33277) in 2% methylcellulose (experimental group) or 2%
579 methylcellulose in PBS (control group) was administered into the oral cavity three times per week for 22 weeks,
580 starting at the age of six months. At the age of 12 months, mice were sacrificed by CO_2 inhalation followed by

581 blood withdrawal and were then transcardially perfused with PBS (pH 7.4). Sample collection and preparation
582 for immunofluorescence staining was carried out according to Barendrecht et al 2023.
583

584 **Immunofluorescent staining**

585 The staining was performed on free-floating 30 μm sagittal brain sections. Sections were incubated with TBS,
586 0.3% Triton-X-100, 5% normal goat serum for 30 min followed by the incubation with Iba-1 (1:250; FUJIFILM
587 Wako Pure Chemical Corporation, Japan) at 4°C overnight in a humid chamber. The following day sections
588 were washed with TBS and incubated with Cy3-labelled goat anti-rabbit secondary antibody (1:250, Dianova)
589 for 60 min. After washing with TBS, the sections were placed under the microscope on slides coated with
590 protein glycerol, air-dried and mounted in mounting media.
591

592 **Fluorescence microscopy**

593 Stained brain tissue sections were examined with an AxioScan.Z1 microscope (Zeiss, Göttingen, Germany)
594 equipped with a Colibri 7 light source. Excitation / Emission filters for Cy3 were at 555 and 595 nm,
595 respectively. Pictures were taken by means of Axiocam 506 and a Plan-Apochromat objective (20×/0.8) and
596 exposure time of 20 ms for Cy3. Images were digitized by means of ZEN blue 3.4 software. Brain regions of
597 interest (cortex and hippocampus) were extracted before microglia analysis by using this software.
598

599 **Microglia Analysis**

600 All immunofluorescence images were processed by a developed macro for ImageJ/Fiji[67,68]. In a preprocessing
601 step, the Cy3 channel was normalized and enhanced in contrast as well as cleaned of artifacts from the stitching
602 procedure of the slide scanner or uneven illumination. The Cy3 channel was binarized with a local mean
603 thresholding algorithm using the same set of parameters for every single image. In the last step, information
604 from the channels is being extracted regarding the object's sizes and the count of objects for each image with
605 the ImageJ/Fiji tool *Analyze Particles*.
606

607 **Tissue staining**

608 Tissue slides were thawed by first incubating at −20°C for 2 hours, followed by 20 min at 4°C. OCT compound
609 was removed by brief incubation in PBS at 4°C. Subsequently, antigen retrieval was performed using EnVision
610 FLEX Target Retrieval Solution High pH (Agilent Dako, K8004; pH = 9), incubated for 15 min at 96°C. Slides
611 were then cooled down to 65°C, briefly rinsed in PBS at room temperature (RT), and permeabilized by
612 incubation in PBS containing 0.5% Triton X-100 for 20 min at RT. Following a PBS wash, tissues were blocked
613 in 4% BSA in PBS for 1 hour at RT.
614 After blocking, samples were stained with a freshly prepared antibody cocktail (Supplementary Table 2), diluted
615 in 0.5% BSA in PBS, and incubated for 20 hours at 4°C. Unbound antibodies were removed through two
616 sequential 8-minute washes in PBS containing 0.5% Triton X-100 with gentle agitation. Finally, nuclei were
617 stained for 20 min in RT with Cell-ID Intercalator at 156 nM in PBS. Slides were then washed twice in Mili-Q
618 water and air-dried.
619

620 **Scanning**

621 Tissues were scanned using Hyperion Imaging System (Standard Biotools) coupled with a Helios mass
622 spectrometer (Standard Biotools), CyTOF software (version 7.1.16401.0). Complete hippocampus area (1.19
623 mm^2) and two regions of interest (ROIs, area 1.19 mm^2 each) from the cerebral cortex dorsal to hippocampus
624 were scanned. Tissue ablation was performed at 1 dB power with a frequency of 200 Hz and an X–Y step size
625 of 1 px (1 px = 1 μm), corresponding to the maximum resolution of the instrument. Signal intensities from
626 each channel were recorded for every scanned pixel and exported as .txt files for further processing.
627

628 **Spillover correction and denoising**

629 A compensation matrix was generated using an in-house antibody microarray. Individual air-dried antibody
630 droplets were scanned, and background signals were measured across all other panel channels, as previously

631 described[69]. Raw intensity data were imported and asinh-transformed with a cofactor of 5. Pixel-level
632 debarcoding was performed using the CATALYST (v1.28.0) package. Misidentified pixels were removed, and
633 spillover was quantified using a channel-wise compensation matrix (Supplementary Fig. 2A).
634 .txt files were processed using the steinbock pipeline. Files were converted to .tiff format with hot pixel filtering
635 set to 50. Images were subsequently loaded using imcRtools (v1.10.0) and cytomapper (v1.16.0). Signal spillover
636 was corrected across all channels except Ir191 and Ir193, using the previously generated matrix. Both pre- and
637 post-compensation images were visually inspected for artifacts and saved as 32-bit .tiff files.
638 Denoising and background removal were performed using the self-supervised IMC-Denoise package[70]. IMC-
639 Denoise environment was created (python 3.6, tensorflow 2.2.0, keras 2.3.1). A randomized subset of 20 ROIs
640 was used for training. Model performance was visually assessed in channels with signal loss exceeding 0.02
641 normalized intensity. Channels CD274, SiglecF, and MHCII were excluded from denoising due to insufficient
642 signal-to-noise contrast.
643

644 **Object segmentation**

645 Cell segmentation was performed using a hybrid Ilastik–CellProfiler workflow[71–73]. Random 250 × 250 px
646 patches were generated from spillover-corrected and denoised images for pixel classifier training in Ilastik
647 (v1.4.0). Three probability channels were defined using visually validated thresholds: channel 1 (nuclei) - trained
648 with Ir193/Ir195 channels in training patches (signal threshold: 37), channel 2 (cytoplasm) - trained with NeuN
649 (signal threshold: 6), GFAP (signal threshold: 23), Iba1 (signal threshold: 9), S100B^{HIGH} (signal threshold: 23)
650 and GLUT1^{HIGH} (signal threshold: 21); and channel 3 as background channel. The resulting probability maps
651 (Supplementary Fig. 2B) were then imported into CellProfiler (v4.2.7) using custom pipelines derived from the
652 steinbock package. The nuclei channel was used as a seed (object size: 3–25 px) for cytoplasmic mask
653 propagation (Supplementary Fig. 2B). To preserve the morphological features of CNS cells, the "Fill holes in
654 identified objects" function was disabled during segmentation.
655 Protein aggregates segmentation was performed in a smiliar manner. Ilastik was used to generate probability
656 maps: channel 1 was pTau^{HIGH} regions, channel 2 - amyloid^{HIGH}, and channel 3 as background. Subsequently,
657 these probability maps were imported into CellProfiler, where the combined signal from Channels 1 and 2 was
658 utilized for precise identification and segmentation of protein aggregates.
659

660 **Data cleanup**

661 The processing workflow was adapted from Windhager et al. with modifications[74].
662 Properties of objects identified as described above were evaluated using the tools in the steinbock package
663 (0.16.1). In short, object intensities and sizes were measured and exported to csv file. Data (tiff images,
664 segmentation masks and single-cell data) were read in Rstudio environment (R 4.4.3, Rstudio 2024.12.1 Build
665 563). Signal was asinh-transformed (co-factor =1), and signal-to-noise ratios were quality checked. Objects with
666 areas smaller than 4 px or larger than 2500 px (cell-like segmentation) or larger than 3000px (aggregates) were
667 excluded from downstream analyses. UMAP dimensionality reduction was performed using scater (v1.32.1) on
668 all markers except DNA1/2. Batch correction was conducted using Seurat v.5.2.0 and SeuratObject v.5.0.2
669 packages[75]. Data were split by slide ID, integrated via reciprocal PCA (k = 20), and reduced to principal
670 components for batch-corrected UMAP generation. Batch-corrected integration quality was visually assessed
671 (Supplementary Fig. 2C).
672 Aggregate segmentation data were batch-corrected using harmony v.1.2.3[76], which exhibited improved
673 biological fidelity compared to Seurat in this context (Supplementary Fig. 5). PCA computations were supported
674 by BiocSingular.
675

676 **Clustering**

677 Cell and protein aggregate typing were performed through unsupervised clustering using the Rphenograph
678 package (v.0.99.1.9003)[66]. The initial clusters from the cell dataset were annotated at k=50 for n = 78 622
679 events. The resulting initial clusters were sorted into the following cell types (hence called metaclusters) based
680 on known patterns of marker expressions: neurons (NeuN^{HIGH}), blood vessels (GLUT1^{HIGH}), astrocytes
681 (GFAP^{HIGH}), microglia (Iba1^{HIGH}), mural cells (CD13/Cox2^{HIGH}) or other cell types that did not distinctly

682 match any of these predefined categories. Due to imaging resolution constraints (minimum scan resolution of
683 1 μm), some degree of antigen signal overlap or cross-contamination (i.e. $GFAP^+$ in $Iba1^{HIGH}$ cell types) was
684 considered acceptable and did not preclude accurate annotation. Subsequently, microglia-like objects from the
685 broader dataset were isolated and further subclustered using Rphenograph with k = 60, resulting in the
686 identification of 21 distinct microglial subclusters.
687 Aggregate typing was performed similarly using Rphenograph (k = 60, n = 60 258). Aggregates were then
688 systematically assigned one of four categorical labels based on specific marker positivity profiles: amyloid
689 ($amyloid^+$, but $pTau^-$ objects), pTau ($pTau^+$, $NeuN^-$), pTau_d ($pTau^+$ and $NeuN^+$) or mixed aggregate ($amyloid^+$
690 and $pTau^+$).
691

692 **Spatial interactions**

693 Cell-to-cell interactions were evaluated by constructing spatial graphs using imcRtools' buildSpatialGraph
694 function, with an expansion threshold of 40 px. For each object, neighboring cells were identified and annotated
695 according to their metacluster classification, which enabled the organization of cells into six distinct regional
696 microenvironments. The compositional structure of these regions—both at the level of broad metaclusters and
697 finer microglial subtypes - was visualized using the lisaClust package[77].
698 Next, region-to-region spatial contexts (SCs) were defined using a k-nearest neighbor (k-NN) approach (k =
699 40). To ensure representation across multiple samples, only SCs with ≥200 total cells and identified in ≥5 ROIs
700 were retained.
701 To quantify interactions between defined clusters—including interactions between cells and protein aggregates
702 - proximity-based analysis was performed using the testInteractions function within imcRtools package, based
703 on proximity expansions (k = 40) in 3-cell-radius patches. Resulting interaction scores were color-coded
704 according to the summed significance values (sigval), with positive enrichment interactions visualized in red
705 and spatial avoidance represented in blue.
706

707 **Aggregate proximity analysis**

708 To characterize the cellular composition surrounding pathological protein aggregates, datasets were merged
709 following cell and aggregate clustering. High-density amyloid and pTau regions were identified using the
710 patchDetection function in *imcRtools*, with detection thresholds set at ≥1.5× the relative signal intensity for
711 amyloid and ≥2.35× for pTau. A minimum patch size of 6 pixels was applied, followed by a 2-pixel expansion
712 to encompass neighboring structures. Patch boundaries were validated by comparing patch area distributions
713 against the corresponding segmented object sizes, ensuring consistency in detection criteria.
714 To assess spatial proximity between cells and pathological regions, distances from each segmented cell object
715 to the nearest aggregate patch were calculated using the plotSpatial function. Distance distributions were then
716 stratified by cell type, enabling comparative analyses of microglial, astrocytic, and neuronal positioning relative
717 to amyloid or pTau pathology.
718

719 **Statistical analysis and data visualisation**

720 Cluster abundance distributions were first assessed for normality using the Shapiro–Wilk test. As most datasets
721 did not meet the assumption of normality, non-parametric Kruskal–Wallis tests were applied for group
722 comparisons, followed by Dunn's post hoc correction. P-values were adjusted for multiple testing (Padj).
723 Statistical analyses were performed using stats v4.4.3, FSA v0.9.6 with dplyr v1.1.4 for necessary data
724 transformations.
725 For data visualisation, GraphPad Prism v.10 or the following R packages were employed: cowplot v1.1.3,
726 dittoSeq v1.16.0, ggplot2 v3.5.1, ggridges v0.5.6, pheatmap v1.0.12. Parallel computations were performed with
727 BiocParallel v1.38.0. All R packages were downloaded and installed through Bioconductor project
728 (BiocManager v1.30.25).
729

730 **Data availability statement**

731 Cytof and IMC datasets have been deposited at doi.org/10.57903/UJ/MQOATZ.

Code availability statement

All R scripts have been deposited at github.com/Dorlana/MicrogliaRush2025.

Funding information

This project has been supported by the EU Join Programme ERA-NET JPND/JPco-fuND2 – Neurodegenerative Disease Research (Gums and Brains project awarded to JP, PM, and HC), the Polish National Science Centre (2019/01/Y/NZ1/00016 to JP), Research Council of Norway (296129 awarded to PM) and Norwegian Health Association, Norway (nr 35318 awarded to MK). MK was supported by the Meltzer Foundation, Norway, and MK, ND and PM were supported by the Broegelmann Research Foundation, Norway.

Generation of tau-KI mice was supported by the Alzheimer's Association (grant: 2016-NIRG-396-583).

Acknowledgements

The authors thank Prof. Steffen Rossner and Dr. Corinna Höfling from Paul Flechsig Institute for Brain Research, University of Leipzig, Germany for help with scanning fluorescent brain sections.

Mass cytometry was performed at the Flow Cytometry Core Facility, University of Bergen.

REFERENCES

1. Scheltens, P. *et al.* Alzheimer's disease. *Lancet Lond. Engl.* **397**, 1577–1590 (2021).
2. Hansen, D. V., Hanson, J. E. & Sheng, M. Microglia in Alzheimer's disease. *J. Cell Biol.* **217**, 459–472 (2018).
3. Hemonnot-Girard, A.-L. *et al.* Comparative analysis of transcriptome remodeling in plaque-associated and plaque-distant microglia during amyloid-β pathology progression in mice. *J. Neuroinflammation* **19**, 234 (2022).
4. Chen, Y. & Colonna, M. Microglia in Alzheimer's disease at single-cell level. Are there common patterns in humans and mice? *J. Exp. Med.* **218**, e20202717 (2021).
5. Butovsky, O., Talpalar, A. E., Ben-Yaakov, K. & Schwartz, M. Activation of microglia by aggregated beta-amyloid or lipopolysaccharide impairs MHC-II expression and renders them cytotoxic whereas IFN-gamma and IL-4 render them protective. *Mol. Cell. Neurosci.* **29**, 381–393 (2005).
6. Abutbul, S. *et al.* TGF-β signaling through SMAD2/3 induces the quiescent microglial phenotype within the CNS environment. *Glia* **60**, 1160–1171 (2012).
7. Dvir-Szternfeld, R. *et al.* Alzheimer's disease modification mediated by bone marrow-derived macrophages via a TREM2-independent pathway in mouse model of amyloidosis. *Nat. Aging* **2**, 60–73 (2022).
8. Laporte, V., Ait-Ghezala, G., Volmar, C.-H. & Mullan, M. CD40 deficiency mitigates Alzheimer's disease pathology in transgenic mouse models. *J. Neuroinflammation* **3**, 3 (2006).
9. Norden, D. M., Fenn, A. M., Dugan, A. & Godbout, J. P. TGFβ produced by IL-10 redirected astrocytes attenuates microglial activation. *Glia* **62**, 881–895 (2014).
10. Fragoso-Morales, L. G., Correa-Basurto, J. & Rosales-Hernández, M. C. Implication of Nicotinamide Adenine Dinucleotide Phosphate (NADPH) Oxidase and Its Inhibitors in Alzheimer's Disease Murine Models. *Antioxid. Basel Switz.* **10**, 218 (2021).
11. Rangan, P. *et al.* Fasting-mimicking diet cycles reduce neuroinflammation to attenuate cognitive decline in Alzheimer's models. *Cell Rep.* **40**, 111417 (2022).
12. Dominy, S. S. *et al.* Porphyromonas gingivalis in Alzheimer's disease brains: Evidence for disease causation and treatment with small-molecule inhibitors. *Sci. Adv.* (2019)
13. Jiang, M. *et al.* GSK3β is involved in promoting Alzheimer's disease pathologies following chronic systemic exposure to Porphyromonas gingivalis lipopolysaccharide in amyloid precursor proteinNL-F/NL-F knock-in mice. *Brain. Behav. Immun.* **98**, 1–12 (2021).

14. Ma, X., Shin, Y.-J., Yoo, J.-W., Park, H.-S. & Kim, D.-H. Extracellular vesicles derived from Porphyromonas gingivalis induce trigeminal nerve-mediated cognitive impairment. *J. Adv. Res.* **54**, 293–303 (2023).
15. Zhu, J., Li, M., Li, J. & Wu, J. Sialic acid metabolism of oral bacteria and its potential role in colorectal cancer and Alzheimer's disease. *Carbohydr. Res.* **541**, 109172 (2024).
16. Schäffer, C. & Andrukhov, O. The intriguing strategies of Tannerella forsythia's host interaction. *Front. Oral Health* **5**, 1434217 (2024).
17. Sparks Stein, P. *et al.* Serum antibodies to periodontal pathogens are a risk factor for Alzheimer's disease. *Alzheimers Dement. J. Alzheimers Assoc.* **8**, 196–203 (2012).
18. Liu, S., Dashper, S. G. & Zhao, R. Association Between Oral Bacteria and Alzheimer's Disease: A Systematic Review and Meta-Analysis. *J. Alzheimers Dis. JAD* **91**, 129–150 (2023).
19. Karaduran, K., Aydogdu, A., Gelisin, O. & Gunpinar, S. Investigating the potential clinical impact of periodontitis on the progression of Alzheimer's disease: a prospective cohort study. *Clin. Oral Investig.* **28**, 67 (2023).
20. Liu, G. *et al.* Measuring the subgingival microbiota in periodontitis patients: Comparison of the surface layer and the underlying layers. *Microbiol. Immunol.* **64**, 99–112 (2020).
21. Park, O.-J. *et al.* Pyrosequencing Analysis of Subgingival Microbiota in Distinct Periodontal Conditions. *J. Dent. Res.* **94**, 921–927 (2015).
22. He, J., Liu, Y., Xu, H., Wei, X. & Chen, M. Insights into the variations in microbial community structure during the development of periodontitis and its pathogenesis. *Clin. Oral Investig.* **28**, 675 (2024).
23. Darveau, R. P. Periodontitis: a polymicrobial disruption of host homeostasis. *Nat. Rev. Microbiol.* **8**, 481–490 (2010).
24. Passariello, C. *et al.* Evaluation of microbiota associated with Herpesviruses in active sites of generalized aggressive periodontitis. *Ann. Stomatol. (Roma)* **8**, 59–70 (2017).
25. Herrero-Sánchez, A. & Haroyan-Darbinyan, E. Prevalence of Epstein-Barr Virus, Cytomegalovirus, and Periodontopathic Bacteria in Patients With Periodontitis: A Case-Control Study. *Clin. Exp. Dent. Res.* **11**, e70084 (2025).
26. Jabri, B., Iken, M., Achmit, M., Rida, S. & Ennibi, O. K. Occurrence of Candida albicans in Periodontitis. *Int. J. Dent.* **2021**, 5589664 (2021).
27. Hajishengallis, G. & Lambris, J. D. More than complementing Tolls: complement-Toll-like receptor synergy and crosstalk in innate immunity and inflammation. *Immunol. Rev.* **274**, 233–244 (2016).
28. Isola, G., Polizzi, A., Santonocito, S., Alibrandi, A. & Williams, R. C. Periodontitis activates the NLRP3 inflammasome in serum and saliva. *J. Periodontol.* **93**, 135–145 (2022).
29. Gong, T. *et al.* Outer membrane vesicles of Porphyromonas gingivalis trigger NLRP3 inflammasome and induce neuroinflammation, tau phosphorylation, and memory dysfunction in mice. *Front. Cell. Infect. Microbiol.* **12**, 925435 (2022).
30. Dadwal, S. & Heneka, M. T. Microglia heterogeneity in health and disease. *FEBS Open Bio* **14**, 217–229 (2024).
31. Nagamoto-Combs, K., Kulas, J. & Combs, C. K. A novel cell line from spontaneously immortalized murine microglia. *J. Neurosci. Methods* **233**, 187–198 (2014).
32. Haditsch, U. *et al.* Alzheimer's Disease-Like Neurodegeneration in Porphyromonas gingivalis Infected Neurons with Persistent Expression of Active Gingipains. *J. Alzheimers Dis.* **75**, 1361–1376 (2020).
33. Chuang, W. *et al.* The mechanisms of Porphyromonas gingivalis-derived outer membrane vesicles-induced neurotoxicity and microglia activation. *J. Dent. Sci.* **19**, 1434–1442 (2024).
34. Sabbagh, M. N. & Decourt, B. COR388 (atuzaginstat): an investigational gingipain inhibitor for the treatment of Alzheimer disease. *Expert Opin. Investig. Drugs* **31**, 987–993 (2022).
35. Faraoni, E. Y. *et al.* CD73-Dependent Adenosine Signaling through Adora2b Drives Immunosuppression in Ductal Pancreatic Cancer. *Cancer Res.* **83**, 1111–1127 (2023).
36. Barendrecht, S. *et al.* A novel human tau knock-in mouse model reveals interaction of Abeta and human tau under progressing cerebral amyloidosis in 5xFAD mice. *Alzheimers Res. Ther.* **15**, 16 (2023).
37. Pettas, S. *et al.* Profiling Microglia through Single-Cell RNA Sequencing over the Course of Development, Aging, and Disease. *Cells* **11**, 2383 (2022).

38. Masuda, T., Sankowski, R., Staszewski, O. & Prinz, M. Microglia Heterogeneity in the Single-Cell Era. *Cell Rep.* **30**, 1271–1281 (2020).
39. Tan, Y.-L., Yuan, Y. & Tian, L. Microglial regional heterogeneity and its role in the brain. *Mol. Psychiatry* **25**, 351–367 (2020).
40. Huang, Y., Tian, C., Li, Q. & Xu, Q. TET1 Knockdown Inhibits Porphyromonas gingivalis LPS/IFN-γ-Induced M1 Macrophage Polarization through the NF-κB Pathway in THP-1 Cells. *Int. J. Mol. Sci.* **20**, 2023 (2019).
41. Nie, R. *et al.* Porphyromonas gingivalis Infection Induces Amyloid-β Accumulation in Monocytes/Macrophages. *J. Alzheimers Dis.* **72**, 479–494 (2019).
42. Liu, Y. *et al.* Infection of microglia with Porphyromonas gingivalis promotes cell migration and an inflammatory response through the gingipain-mediated activation of protease-activated receptor-2 in mice. *Sci. Rep.* **7**, 11759 (2017).
43. Nonaka, S. & Nakanishi, H. Secreted gingipains from Porphyromonas gingivalis induce microglia migration through endosomal signaling by protease-activated receptor 2. *Neurochem. Int.* **140**, 104840 (2020).
44. Li, X. *et al.* Porphyromonas gingivalis promote microglia M1 polarization through the NF-κB signaling pathway. *Heliyon* **10**, e35340 (2024).
45. Yang, J., Wise, L. & Fukuchi, K.-I. TLR4 Cross-Talk With NLRP3 Inflammasome and Complement Signaling Pathways in Alzheimer's Disease. *Front. Immunol.* **11**, 724 (2020).
46. Sanjay, Shin, J.-H., Park, M. & Lee, H.-J. Cyanidin-3-O-Glucoside Regulates the M1/M2 Polarization of Microglia via PPARγ and Aβ42 Phagocytosis Through TREM2 in an Alzheimer's Disease Model. *Mol. Neurobiol.* **59**, 5135–5148 (2022).
47. Szaingurten-Solodkin, I., Hadad, N. & Levy, R. Regulatory role of cytosolic phospholipase A2alpha in NADPH oxidase activity and in inducible nitric oxide synthase induction by aggregated Abeta1-42 in microglia. *Glia* **57**, 1727–1740 (2009).
48. Clayton, K. *et al.* Plaque associated microglia hyper-secrete extracellular vesicles and accelerate tau propagation in a humanized APP mouse model. *Mol. Neurodegener.* **16**, 18 (2021).
49. Grubman, A. *et al.* Transcriptional signature in microglia associated with Aβ plaque phagocytosis. *Nat. Commun.* **12**, 3015 (2021).
50. Lim, Y., Kim, H. Y., An, S.-J. & Choi, B.-K. Activation of bone marrow-derived dendritic cells and CD4+ T cell differentiation by outer membrane vesicles of periodontal pathogens. *J. Oral Microbiol.* **14**, 2123550 (2022).
51. Kummer, M. P. *et al.* Microglial PD-1 stimulation by astrocytic PD-L1 suppresses neuroinflammation and Alzheimer's disease pathology. *EMBO J.* **40**, e108662 (2021).
52. Rosenzweig, N. *et al.* PD-1/PD-L1 checkpoint blockade harnesses monocyte-derived macrophages to combat cognitive impairment in a tauopathy mouse model. *Nat. Commun.* **10**, 465 (2019).
53. Wu, C.-T. *et al.* A change of PD-1/PD-L1 expression on peripheral T cell subsets correlates with the different stages of Alzheimer's Disease. *Cell Biosci.* **12**, 162 (2022).
54. Schachtele, S. J., Hu, S., Sheng, W. S., Mutnal, M. B. & Lokensgard, J. R. Glial cells suppress postencephalitic CD8+ T lymphocytes through PD-L1. *Glia* **62**, 1582–1594 (2014).
55. Fekete, R. *et al.* Microglia dysfunction, neurovascular inflammation and focal neuropathologies are linked to IL-1- and IL-6-related systemic inflammation in COVID-19. *Nat. Neurosci.* **28**, 558–576 (2025).
56. Yang, A. C. *et al.* Dysregulation of brain and choroid plexus cell types in severe COVID-19. *Nature* **595**, 565–571 (2021).
57. Martins-Ferreira, R. *et al.* The Human Microglia Atlas (HuMicA) unravels changes in disease-associated microglia subsets across neurodegenerative conditions. *Nat. Commun.* **16**, 739 (2025).
58. Fujikura, M. *et al.* CD14 and Toll-Like Receptor 4 Promote Fibrillar Aβ42 Uptake by Microglia Through A Clathrin-Mediated Pathway. *J. Alzheimers Dis. JAD* **68**, 323–337 (2019).
59. Pereira, J. B. *et al.* Microglial activation protects against accumulation of tau aggregates in nondemented individuals with underlying Alzheimer's disease pathology. *Nat. Aging* **2**, 1138–1144 (2022).
60. Hammond, T. R. *et al.* Single-Cell RNA Sequencing of Microglia throughout the Mouse Lifespan and in the Injured Brain Reveals Complex Cell-State Changes. *Immunity* **50**, 253-271.e6 (2019).

886 61. Silvin, A. *et al.* Dual ontogeny of disease-associated microglia and disease inflammatory macrophages in
887 aging and neurodegeneration. *Immunity* **55**, 1448-1465.e6 (2022).
888 62. Wendimu, M. Y. & Hooks, S. B. Microglia Phenotypes in Aging and Neurodegenerative Diseases. *Cells*
889 **11**, 2091 (2022).
890 63. Takasugi, M. *et al.* An atlas of the aging mouse proteome reveals the features of age-related post-
891 transcriptional dysregulation. *Nat. Commun.* **15**, 8520 (2024).
892 64. Ghazalpour, A. *et al.* Comparative Analysis of Proteome and Transcriptome Variation in Mouse. *PLoS*
893 *Genet.* **7**, e1001393 (2011).
894 65. Dick, F., Tysnes, O.-B., Alves, G. W., Nido, G. S. & Tzoulis, C. Altered transcriptome-proteome
895 coupling indicates aberrant proteostasis in Parkinson's disease. *iScience* **26**, 105925 (2023).
896 66. Levine, J. H. *et al.* Data-Driven Phenotypic Dissection of AML Reveals Progenitor-like Cells that
897 Correlate with Prognosis. *Cell* **162**, 184–197 (2015).
898 67. Schindelin, J. *et al.* Fiji: an open-source platform for biological-image analysis. *Nat. Methods* **9**, 676–682
899 (2012).
900 68. Gnoth, K. *et al.* Evidence for Enhanced Efficacy of Passive Immunotherapy against Beta-Amyloid in
901 CD33-Negative 5xFAD Mice. *Biomolecules* **12**, 399 (2022).
902 69. Chevrier, S. *et al.* Compensation of Signal Spillover in Suspension and Imaging Mass Cytometry. *Cell Syst.*
903 **6**, 612-620.e5 (2018).
904 70. Lu, P. *et al.* IMC-Denoise: a content aware denoising pipeline to enhance Imaging Mass Cytometry. *Nat.*
905 *Commun.* **14**, 1601 (2023).
906 71. Berg, S. *et al.* ilastik: interactive machine learning for (bio)image analysis. *Nat. Methods* **16**, 1226–1232
907 (2019).
908 72. Stirling, D. R. *et al.* CellProfiler 4: improvements in speed, utility and usability. *BMC Bioinformatics* **22**, 433
909 (2021).
910 73. Carpenter, A. E. *et al.* CellProfiler: image analysis software for identifying and quantifying cell
911 phenotypes. *Genome Biol.* **7**, R100 (2006).
912 74. Windhager, J. *et al.* An end-to-end workflow for multiplexed image processing and analysis. *Nat. Protoc.*
913 **18**, 3565–3613 (2023).
914 75. Stuart, T. *et al.* Comprehensive Integration of Single-Cell Data. *Cell* **177**, 1888-1902.e21 (2019).
915 76. Korsunsky, I. *et al.* Fast, sensitive and accurate integration of single-cell data with Harmony. *Nat. Methods*
916 **16**, 1289–1296 (2019).
917 77. Patrick, E. *et al.* Spatial analysis for highly multiplexed imaging data to identify tissue microenvironments.
918 *Cytom. Part J. Int. Soc. Anal. Cytol.* **103**, 593–599 (2023).
919

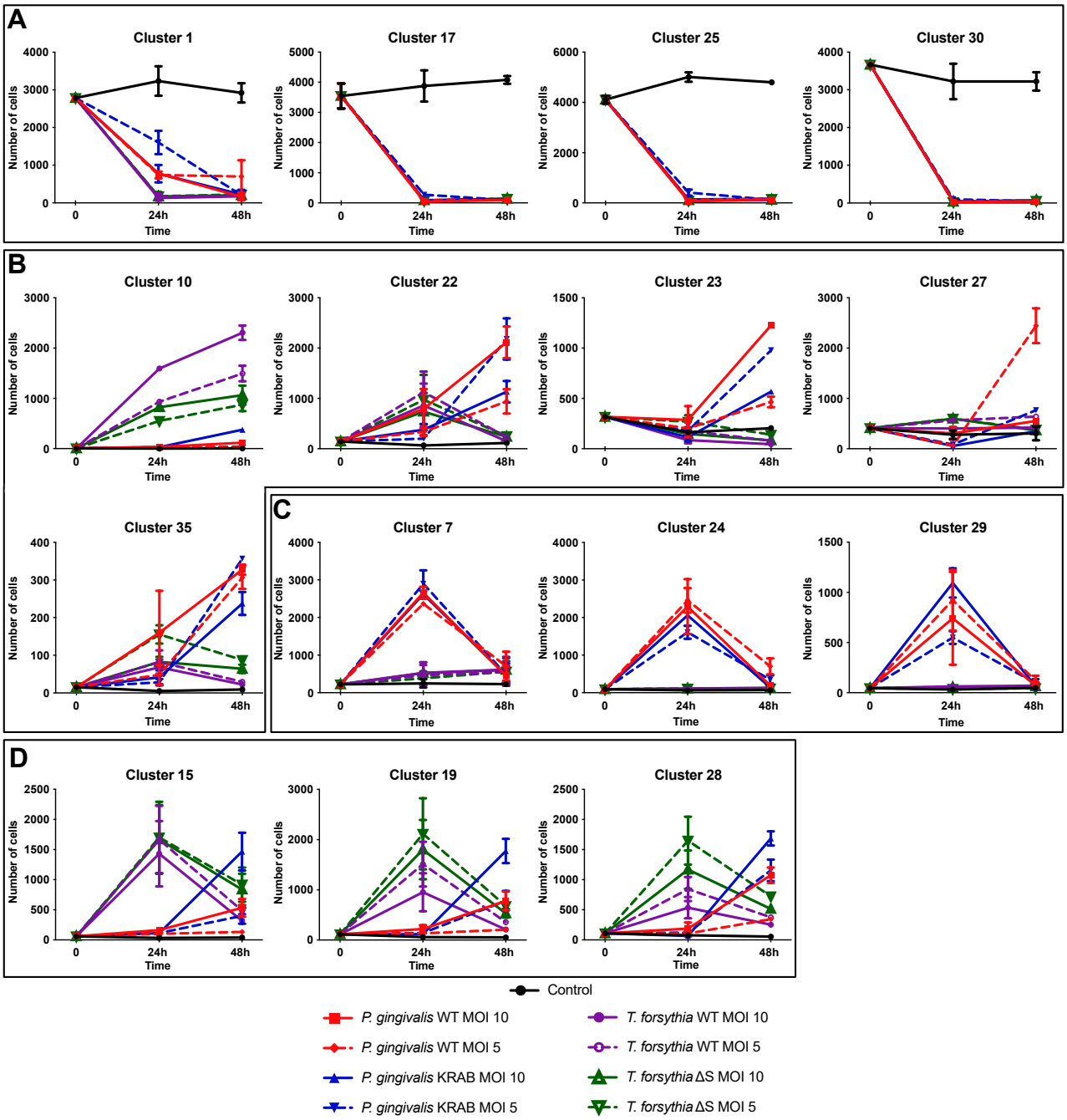

Extended Data Figure 1. Temporal dynamics of SIM-A9 microglial clusters following infection with *P. gingivalis* or *T. forsythia*.

Line plots show relative abundance of selected clusters across conditions at 0 h (untreated), and 24 h and 48 h post-infection, following downsampling to equal cell numbers per condition. Each point represents mean of biological replicates ± SEM; lines connect mean values.

A. Clusters 1, 17, 25 and 30. **B.** Clusters 10, 22, 23, 27 and 35. **C.** Clusters 7, 24 and 29. **D.** Clusters 15, 19 and 28. **E.** Clusters 26 and 31.

Color-coded legend indicates treatment conditions and pathogen strains (MOI 5 or 10), as in Fig. 2. Cluster-specific responses show distinct temporal trajectories and pathogen sensitivities. Statistical analyses are shown in Fig. 2b and Methods.

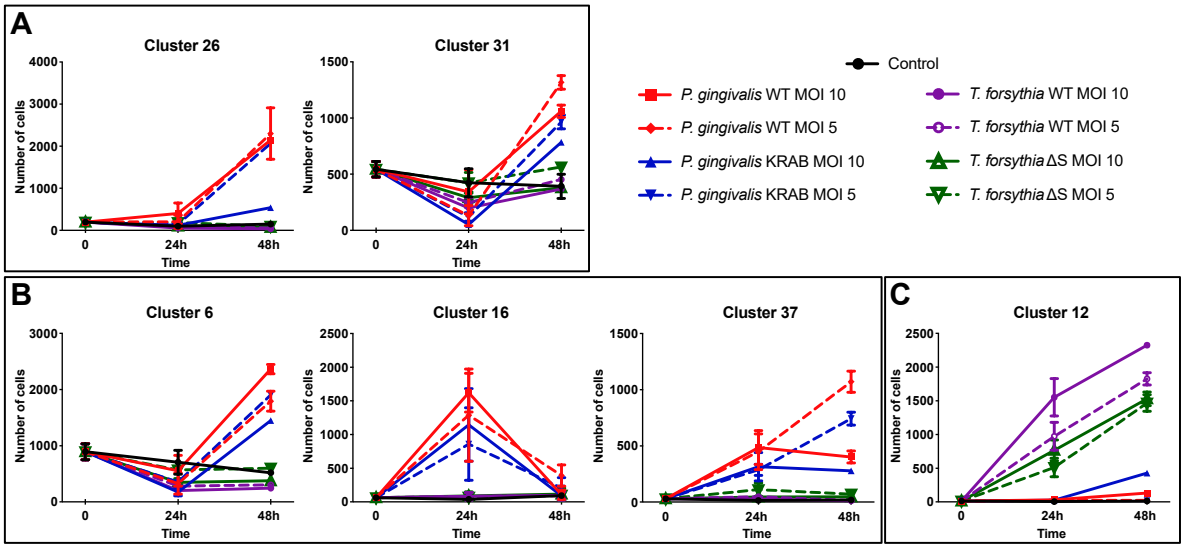

Extended Data Figure 2. Temporal dynamics of SIM-A9 microglial clusters following infection with *P. gingivalis* or *T. forsythia*.

Line plots show relative abundance of selected clusters across conditions at 0 h (untreated), and 24 h and 48 h post-infection, following downsampling to equal cell numbers per condition. Each point represents mean of biological replicates ± SEM; lines connect mean values.

A. Clusters 26 and 31. **B.** Clusters 6, 16 and 37. **C.** Cluster 12.

Color-coded legend indicates treatment conditions and pathogen strains (MOI 5 or 10), as in Fig. 2. Cluster-specific responses show distinct temporal trajectories and pathogen sensitivities. Statistical analyses are shown in Fig. 2b and Methods.

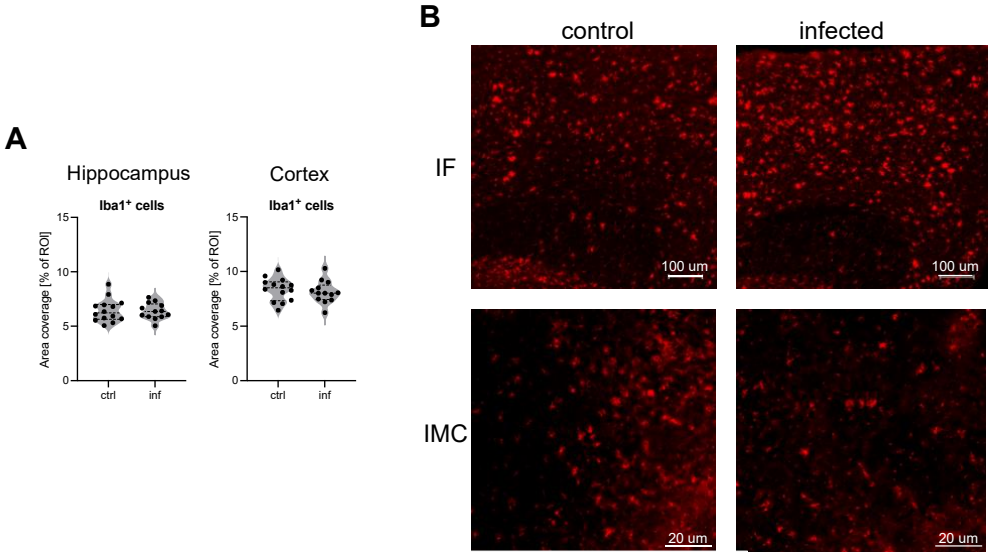

Extended Data Figure 3. Microglial abundance is unaltered by chronic infection: concordant results from immunofluorescence and imaging mass cytometry.

A. Quantification of Iba1$^+$ area in the hippocampus (left) and cerebral cortex (right) shows no significant difference between control and *P. gingivalis*–infected hTau × 5×FAD mice, as assessed by immunofluorescence. Data represent percentage of Iba1$^+$ area per brain region. **B.** Representative images of Iba1$^+$ microglia from both control and infected animals, obtained using immunofluorescence (top; scale bar = 100 μm) and imaging mass cytometry (bottom; scale bar = 20 μm), demonstrate comparable Iba1 signal distribution and morphology across methods. Immunofluorescence staining was performed on free-floating 30 μm sagittal brain sections using anti-Iba1 (1:250, FUJIFILM Wako) and Cy3-conjugated secondary antibody (1:250, Dianova). Sections were mounted in glycerol-based media and imaged using an AxioScan.Z1 microscope (Zeiss) with Cy3 excitation/emission (555/595 nm), a 20×/0.8 Plan-Apochromat objective, and 20 ms exposure time. Image processing was performed using ZEN blue 3.4 software. Microglial area analysis was conducted using a custom ImageJ/Fiji macro. Cy3 channel intensity was normalized and contrast-enhanced, followed by artifact correction and binarization using a local mean thresholding algorithm. Iba1$^+$ area was quantified using the Analyze Particles tool under uniform parameters across all samples. Both immunofluorescence and imaging mass cytometry approaches yielded consistent results, showing no significant differences in regional microglial abundance between experimental groups.